DUST MIGRATION AND MORPHOLOGY IN OPTICALLY THIN CIRCUMSTELLAR GAS DISKS

Taku Takeuchi[1] and Pawel Artymowicz
Stockholm Observatory, Stockholm University, SE-133 36 Saltsjöbaden, Sweden; taku@ucolick.org, pawel@astro.su.se

ABSTRACT

We analyze the dynamics of gas-dust coupling in the presence of stellar radiation pressure in circumstellar disks, which are in a transitional stage between the gas-dominated, optically thick, primordial nebulae, and the dust-dominated, optically thin Vega-type disks. Dust grains undergo radial migration, either leaving the disk owing to a strong radiation pressure or seeking a stable equilibrium orbit in corotation with gas. In our models of A-type stars surrounded by a total gas mass from a fraction to dozens of Earth masses, the outward migration speed of dust is comparable with the gas sound speed. Equilibrium orbits are circular, with exception of those significantly affected by radiation pressure, which can be strongly elliptic with apocenters extending beyond the bulk of the gas disk. The migration of dust gives rise to radial fractionation of dust and creates a variety of possible observed disk morphologies, which we compute by considering the equilibrium between the dust production and the dust-dust collisions removing particles from their equilibrium orbits. Large grains (typically $\gtrsim 200$ μm) are distributed throughout most of the gas disk. Smaller grains (in the range of 10–200 μm) concentrate in a prominent ring structure in the outer region of the gas disk (presumably at radius ~ 100 AU), where gas density is rapidly declining with radius. The width and density, as well as density contrast of the dust ring with respect to the inner dust disk, depend on the distribution of gas and the mechanical strength of the particles. Our results open the prospect for deducing the distribution of gas in circumstellar disks by observing their dust. We have qualitatively compared our models with two observed transitional disks around HR 4796A and HD 141569A. Dust migration can result in observation of a ring or a bimodal radial dust distribution, possibly very similar to the ones produced by gap-opening planets embedded in the disk, or shepherding it from inside or outside. We conclude that a convincing planet detection via dust imaging should include specific nonaxisymmetric structure (spiral waves, streamers, resonant arcs) following from the dynamical simulations of perturbed disks.

Subject headings: accretion, accretion disks — circumstellar matter — planetary systems: formation — solar system: formation — stars: formation

1. INTRODUCTION

Dust and gas disks surround stars of different ages, from pre–main-sequence to post–main-sequence stars. Because their evolution is intimately connected with the process of planet formation, studies of dust amount, size spectrum, mineralogy, and spatial distribution in disks can provide valuable information about the crucial stages of planet formation.

The amount of dust in disks generally decreases with time (Zuckerman & Becklin 1993; Natta, Grinin, & Mannings 2000). As a consequence, the fraction of detectable optically thick disks decreases from nearly 100% at the estimated object age ~ 0.3 Myr down to a few percent at the age of ~ 10 Myr (Hillenbrand & Meyer 1999; Meyer & Beckwith 2000). The amount of gas decreases as well (Zuckerman, Forveille, & Kastner 1995; Liseau & Artymowicz 1998), especially abruptly at an age of several to ~ 10 Myr for solar-type stars, when circumstellar disks lose most of the primordial protostellar/protoplanetary material through processes such as viscous accretion and photoionization, as discussed by Hollenbach, Yorke, & Johnstone (2000). From the original value of close to 100, the gas-to-solids (if not necessarily gas-to-dust) mass ratio in the T Tauri and Herbig Ae/Be stars decreases during this period (i.e., typically at age 3–10 Myr) to much smaller values, eventually much less than unity, thus leaving a predominantly dusty

remnant disk. Future observations of dust continuum and H_2 molecular lines of disks, e.g., by the Space Infrared Telescope Facility (SIRTF) and the Next Generation Space Telescope (NGST), will help determine the evolution of the gas-to-solid ratio.

Vega-type stars, observable owing to their large thermal infrared (IR) excess over the extrapolated IR stellar photospheric radiation, and sometimes resolved in scattered visible/near-IR starlight, are thought to contain such gas-poor disks. The prime example of an object of this kind is β Pic, which is 20–100 Myr old and has a large disk ($> 10^3$ AU radius) containing gas and dust, apparently in a ratio smaller than unity (Artymowicz 1997; Liseau & Artymowicz 1998; see however Thi et al. 2001). Based on dust destruction timescale in Vega-type disks, the disks are thought (or sometimes defined) to be continuously replenished by the collisions and evaporation of planetesimals. Most convincingly in β Pic, but also in a few younger, spectroscopically variable Herbig Ae stars, the existence of planetesimals and planetary objects necessary to perturb planetesimal orbits, has been inferred from spectroscopy (Lagrange, Backman, & Artymowicz 2000; Grady et al. 2000b).

The disks around stars with ages between 3 and 10 Myr (young main-sequence stars or old pre–main-sequence stars) are particularly interesting because of the expected presence of protoplanets, growing by collisional accumulation of planetesimals and through gas accretion (Hayashi, Nakazawa, & Nakagawa 1985; Lissauer 1993). We shall

[1] Present address: UCO/Lick Observatory, University of California, Santa Cruz, CA 95064.

call such disks transitional, in reference to a transition from a relatively high-mass, optically thick primordial nebulae to low-mass, optically thin dust disks.

Recent imaging of two apparently transitional disks, HR 4796A and HD 141569A, provided interesting insight into the spatial distribution of dust. The A0 V star HR 4796A with age 8 ± 2 Myr (Stauffer, Hartmann, & Barrado y Navascues 1995) has been imaged, first in mid-IR and afterwards in near-IR (Koerner et al. 1998; Jayawardhana et al. 1998; Schneider et al. 1999; Telesco et al. 2000). The second object, B9.5 Ve star HD 141569A, is 5 Myr old (Weinberger et al. 2000). Near-IR images of its dust disk were obtained by Weinberger et al. (1999) and Augereau et al. (1999a), while the thermal mid-IR flux was mapped by Fisher et al. (2000). Both disks show axisymmetric ring structure with inner holes. The radii of the inner holes are ~ 60 AU for HR 4796A and 150–200 AU for HD 141569A. The image of HD 141569A taken at 1.1 μm by Weinberger et al. (1999) has been analyzed to reveal a double ring, or ring-gap-ring morphology with the shallow gap (or dip) at the projected distance $r = 250$ AU. Noteworthy, the same system observed at 1.6 μm by Augereau et al. (1999a) shows only one broad ring peaking in brightness at $r = 325$ AU. We notice that the differences between the images at 1.1 μm and 1.6 μm, so far unexplained, might be due to wavelength-dependent scattering efficiency of dust. (If the inner peak of HD 141569A is dominated by small grains, then it would Rayleigh-scatter 4.5 times better at 1.1 μm than at 1.6 μm.) Recently, HD 163296, a Herbig Ae star, was reported by Grady et al. (2000a) to have a disk-and-gap morphology similar to that of HD 141569A.

Disks around Vega-type stars, which are more evolved than the transitional disks discussed above, also have inner holes or clearing regions. Mid-IR images of the β Pic disk show the central low-density hole (Lagage & Pantin 1994; Pantin, Lagage, & Artymowicz 1997) and submillimeter images of Fomalhaut and ϵ Eridani show the ringlike structure of dust disks (Holland et al. 1998; Greaves et al. 1998). It is expected that the gravity of embedded large bodies, such as planets or brown dwarfs, form such inner holes in the dust distributions (Roques et al. 1994; Liou & Zook 1999; Ozernoy et al. 2000).

The inner holes of the transitional disks around HR 4796A and HD 141569A may also be produced by planetary bodies embedded in the disks. Planetary influences creating the disk "gap" at 250 AU from HD 141569A have been proposed as an explanation of these striking features. Weinberger et al. (1999) estimate that a 1.3 Jupiter mass perturber would open a gap with the observed extent. Grady et al. (2000a) suggest, in turn, the possibility of early formation of massive planets at distances as large as $r > 300$ AU from HD 163296.

However, there are several potential difficulties with the proposal that giant planets form routinely at such large distances in disks, in only several Myr. Notice that the circular orbit of a planet, required by the circularity of a narrow "gap," would imply a local formation history of the hypothetical planet. Formation in the inner disk and ejection to a large distance by, e.g., planet-planet perturbations would not provide a nearly circular orbit required. Admittedly, radial migration of planets via interaction with the disk may also occur but an *outward* migration distance is always moderate. Standard theory of planet formation requires a high surface density of solids for giant planet formation at large radii (Lissauer 1993). Apparently, the

Kuiper belt region outside Neptune was never so dense. For example, the numerical simulations of planetesimal accretion at 70 AU by Kenyon et al. (1999) showed that the Pluto-sized planets (but not the required multi-Earth mass planets) may form in 10 Myr only if the mass of the disk is as large as 10–20 times the minimum solar nebula mass ($M_g \sim 0.2$–0.4 $M_\odot$), a mass about 10 times larger than the typical masses of T Tauri star disks (Osterloh & Beckwith 1995).

A different mode of giant planet formation via the disk fragmentation may occur in the early stage of disk evolution (Boss 2000), although it has not been demonstrated yet what would defeat a self-defense mechanism disks possess against breakup, connected with quick mass redistribution by open spiral arms excited in stable, massive disks (Laughlin & Bodenheimer 1994). One argument against it can be made in the HD 141569A system, where the surface brightness profile does not show any deep depletion of dust (an empty gap) such as those, which quickly appear around a giant planet in hydrodynamical models (e.g., Lubow, Seibert, & Artymowicz 1999). On the contrary, the "gap" is merely a 14% dip in the surface density of dust, as compared with neighboring disk regions. Weinberger et al. (1999) thus propose a very recent timing for the formation of their proposed Jovian perturber. Troublesome as it is for any formation scenario, the special timing of observations seems particularly incompatible with the *very early* disk fragmentation scenarios.

Motivated by the apparent axisymmetry of the ring and gap structures in disks observed so far, we devote this paper to exploratory study of an alternative mechanism for the appearance of a variety of possible dust morphologies including outer dust rings and apparent disk gaps, connected with the phenomenon of radial migration of dust in gas disks. In the context of transitional disks, which are optically thin to the stellar visible and near-UV radiation and have gas component with moderate mass, we consider two important effects: radiation pressure from the central star and gas drag. As we will show, the combination of radiation and drag forces results in an *outward* direction of migration for the observable dust (size $s \lesssim 1$ mm) and strongly affects the observed disk morphology, while preserving the usual inward direction of migration of sand and larger bodies ($s \gtrsim 1$ mm).

It is easy to see why transitional disks support the most vigorous migration. Primordial protoplanetary nebulae are both optically thick and so dense (gas:dust mass ratio $\sim 10^2$) that most dust grains "freeze" in gas and are not able to migrate through the gas. Vega-type stars, on the other hand, are dust-dominated (Lagrange et al. 2000). They generally contain so little gas (gas:dust $\ll 1$) that the motion of dust is weakly affected in the grain's lifetime. In contrast, HR 4796A and HD 141569A may have gas disks comparable with or somewhat more massive than the dust disks. Zuckerman et al. (1995) have found CO line emission from the gas inside 130 AU from HD 141569A. A double Hα line from the gas disk in the immediate vicinity of the star (Dunkin, Barlow, & Ryan 1997) also demonstrates the existence of an extended gas disk, required for sustained accretion of gas. Whether this gas is a remnant of primordial gaseous nebula or a secondary gas released by solids (for instance, evaporating planetesimals), is not known at present. In any cases, transitional disks may have substantial amounts of gas (many Earth masses), even if an unfavorable viewing geometry of most systems precludes a

spectroscopic detection of the circumstellar absorption lines. Artymowicz (2000) argues that gas must be present and gas drag must be operative in the transitional disks, or else the radiation pressure-boosted destruction rate of solids would be prohibitively large.

The most important feature of our model is that at the outer edge of the gas disk, dust forms a ring without the help of any shepherding bodies. Therefore, the ring structure of the dust disk does not necessarily indicate the existence of planets or brown dwarfs. Klahr & Lin (2001) also proposed a model for the ring formation due to the dust migration. These models should be tested quantitatively by all the observational data, taking into account each system's scale, central star's properties, indications of dust mineralogy from spectroscopy etc. We defer such detailed modeling of transitional disks to a later publication, but provide qualitative discussions in § 7. It should, however, be stressed that our model is testable against the existing observations, and can suggest new observations. Excluding dust migration as a cause of the observed disk structure might, in fact, be as important as finding that it matches the observations of a given object, since such an exclusion would strongly support the hypothesis of dynamical sculpting by planets.

The plan of the paper is as follows. In § 2 we describe the equations of the dust grain's motion. In § 3 we derive approximate expressions of radial velocity of grains, showing both inward and outward migrations. In § 4 the segregation of grains in the gas disk according to their sizes is discussed. In § 5 the orbital evolution of grains is calculated numerically. We discuss the excitation of orbital eccentricity at the edge of the gas disk. In § 6 we calculate the lifetime and number density of grains by taking into account the collisional destruction of grains. In § 7 we show a sample image in near- and mid-IR from our simple model. In § 8 we discuss the relevance of the migration-induced dust structures to observed systems and compare them with dust features of other origin.

2. EQUATIONS OF MOTION OF DUST GRAINS IN A GAS DISK

We consider the motion of dust grains in a gas disk. The equation of motion of a dust grain with mass m and the position vector r is

$$m \frac{d^2 r}{dt^2} = - \frac{GMm}{r^2} \hat{r} + F_{\rm rad} + F_{\rm PR} + F_g , \qquad (1)$$

where r is the distance of the grain from the central star, $\hat{r}$ is the unit vector directed to the grain, G is the gravitational constant, M is the central star's mass, and $F_{\rm rad}$, $F_{\rm PR}$, and F_g are the radiation pressure, Poynting-Robertson drag (PR drag), and gas drag force, respectively.

The radiation pressure force $F_{\rm rad}$ is expressed using the ratio of radiation pressure force to the gravitational force β,

$$F_{\rm rad} = \beta \frac{GMm}{r^2} \hat{r} . \qquad (2)$$

The ratio β is written as (Burns, Lamy, & Soter 1979)

$$\beta = \frac{3 L Q_{\rm PR}}{16 \pi G M c s \rho_d} , \qquad (3)$$

where L is the central star's luminosity, c is the speed of light, s is the grain's radius, ρ_d is the material density of the

grain, and $Q_{\rm PR}$ is the radiation pressure coefficient averaged over the stellar spectrum. The values of β are calculated using Mie theory as in Artymowicz (1988) and shown in Figure 1. The grains are assumed to consist of silicates. We use the laboratory measurements of optical constants of olivine ($MgFeSiO_4$) and magnesium-rich pyroxene ($Mg_{0.8}Fe_{0.2}SiO_3$) by Dorschner et al. (1995).[2] The grains are modeled as porous, containing 50% volume fraction of vacuum (the volume fractions of the two silicates being 25% each). The density of composite grains is then $\rho_d = 1.25$ g cm^{-3}. For the central stars, we used parameters of HR 4796A (*solid line*) and HD 141569A (*dashed line*), and the renormalized spectrum of A0 V type star Vega. The mass and luminosity of HR 4796A are $M = 2.5 \, M_\odot$ and $L = 21.0 \, L_\odot$, respectively (Jura et al. 1993; Jura et al. 1998), while for HD 141569A these parameters are $M = 2.3 \, M_\odot$ and $L = 22.4 \, L_\odot$ (van den Ancker et al. 1998).

The PR drag force $F_{\rm PR}$ is

$$F_{\rm PR} = - \beta \frac{GMm}{r^2} \left(\frac{v_r}{c} \hat{r} + \frac{v}{c} \right) , \qquad (4)$$

where v is the velocity vector of the grain, and v_r is the velocity component in the $\hat{r}$ direction (Burns, Lamy, & Soter 1979).

If the velocities of the grain (v) and the gas (v_g) differ, the grain experiences a gas drag force F_g. The sizes of grains considered in this paper are much smaller than the mean free path of the gas molecules. Thus, if the velocity difference $\Delta v = v - v_g$ is much smaller than the mean thermal velocity of gas, the gas drag force is given by the Epstein drag law

$$F_g = - \pi \rho_g s^2 v_T \Delta v , \qquad (5)$$

where ρ_g is the gas density and v_T is 4/3 times the mean thermal velocity. For the gas with mean molecular weight μ_g and temperature T, v_T is

$$v_T = \frac{4}{3} \left(\frac{8 k T}{\pi \mu_g m_{\rm H}} \right)^{1/2} , \qquad (6)$$

where k is Boltzmann's constant and $m_{\rm H}$ is the mass of the hydrogen atom. In the case of $\Delta v = | \Delta v | \gg v_T$, the gas drag

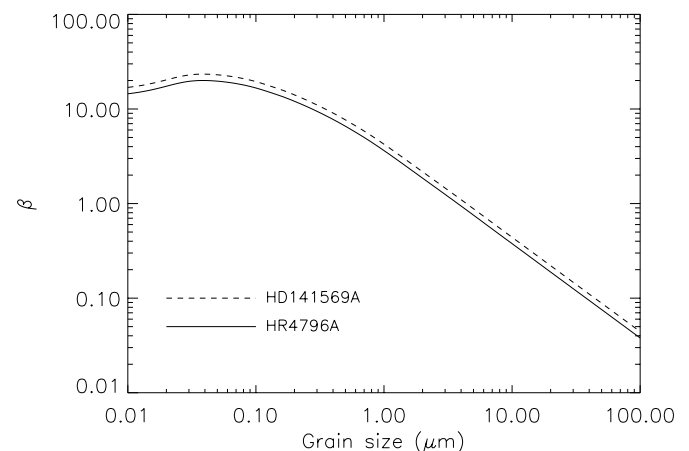[2] Optical data are available from http://www.astro.uni-jena.de/Group/Subgroups/Spectroscopylab/odata.html.

FIG. 1.—Radiation pressure to gravity ratio, β, around HR 4796A (*solid line*) and HD 141569A (*dashed line*).

force is

$$F_g = -\pi\rho_g s^2 \Delta v \Delta v \, . \tag{7}$$

A standard way to connect these two regimes is (Kwok 1975)

$$F_g = -\pi\rho_g s^2 (v_T^2 + \Delta v^2)^{1/2} \Delta v \, . \tag{8}$$

The stopping time by the gas drag force is defined as $t_s = m\Delta v / |F_g|$. It can be made nondimensional by writing $t_s = T_s \Omega_K^{-1}$, where $\Omega_K = (GM/r^3)^{1/2}$ is the Keplerian angular velocity. The nondimensional stopping time can then be expressed as

$$T_s = \frac{T_{ss}}{\sqrt{1 + \Delta v^2 / v_T^2}} \, , \tag{9}$$

where the square-root factor represents the supersonic correction. The subsonic stopping time parameter equals

$$T_{ss} = \frac{4\rho_d s v_K}{3\rho_g r v_T} \, , \tag{10}$$

where $v_K = (GM/r)^{1/2}$ is the Keplerian velocity. When $T_{ss} = 1$, particles move slowly through the gas and couple to it in one dynamical timescale. Such particles are said to be marginally coupled to gas via gas drag, as opposed to the $T_{ss} \gg 1$ case, representing large particles, decoupled from the gas disk. Notice that to within a factor close to unity $\rho_g r v_T / v_K$ equals the gas surface density Σ_g in a disk [$\Sigma_g = (3\pi\sqrt{\Gamma/8})(\rho_g r v_T / v_K)$ for vertically isothermal disks with the mid-plane density ρ_g and the adiabatic exponent Γ]. This allows us to express T_{ss} as $T_{ss} \approx \Sigma_{1p}/\Sigma_g$, the inverse ratio of Σ_g and a "surface density of one solid particle," $\Sigma_{1p} = 4\rho_d s/3$ (mass/cross-sectional area for a spherical particle). For example, a hypothetical uniform surface density gas disk with radius 100 AU and total mass $3 \times 10^{-5} M_\odot$, or 10 Earth masses, would have $\Sigma_g = 8.5 \times 10^{-3}$ g cm^{-2}, the same as the Σ_{1p} of an $s = 51$ μm particle with density $\rho_d = 1.25$ g cm^{-3}. All the dust grains smaller than about 51 μm would then be well coupled to gas in such a disk, while all sand grains ($s \gtrsim 1$mm) would have stopping time much longer than one orbital period.

The velocity of gas v_g can be written using the Keplerian velocity v_K as

$$v_g = v_K (1 - \eta)^{1/2} \, . \tag{11}$$

Quantity η is the ratio of the pressure gradient force to the gravitational force, equal to

$$\eta = -\frac{1}{r\Omega_K^2 \rho_g} \frac{dP_g}{dr} \, , \tag{12}$$

where r is the distance from the central star, and P_g is the gas pressure. If gas pressure decreases with radius, which normally happens everywhere in the disk except at the inner disk edge, $\eta > 0$ and the gas orbital motion is slightly sub-Keplerian, that is slower than v_K.

In this paper, we consider the dust particles near the mid-plane of the gas disk, where we introduce cylindrical coordinates (r, θ), and neglect the fact that the grains might have finite orbital inclinations. This is equivalent to considering the vertical motions to be averaged out by vertical integration over an ensemble of particles in a short column above and below the point (r, θ). This approach is justified by the generally weak coupling of vertical and planar motions of a grain in a thin disk. The radial and azimuthal components of the equation of motion (1) of a dust grain at $r = (r, \theta)$ with velocity $v = (v_r, v_\theta)$ are

$$\frac{dv_r}{dt} = \frac{v_\theta^2}{r} - \frac{v_K^2}{r}\left[1 - \beta\left(1 - \frac{2v_r}{c}\right)\right] - \frac{v_K v_r}{T_s r} \, , \tag{13}$$

$$\frac{d}{dt}(rv_\theta) = -\frac{\beta v_K^2 v_\theta}{c} - \frac{v_K}{T_s}(v_\theta - v_g) \, , \tag{14}$$

where T_s given by equation (9) depends on the velocity of the grain. When the PR and gas drag forces are neglected, the azimuthal velocity of the grain's circular motion is

$$v_\theta = v_K (1 - \beta)^{1/2} \, . \tag{15}$$

If the radiation pressure is strong and $\beta > \eta$, the grain rotates slower than gas (see eqs. [11] and [15]), while grains with negligible β rotate faster than gas.

3. RADIAL MIGRATION OF SOLIDS

Small solid bodies migrate in disks with a speed depending on their size, radiative support and gas drag. If the radiation pressure exceeds central star's gravity ($\beta > 1$), then the grains (called β-meteoroids) are blown away on a dynamical timescale, unless strongly braked by friction against gas. We do not concern ourselves with the observability of rapidly escaping β-meteoroids in this paper. (We do take into account their collisions with stable disk particles, however.) In this section, we consider grains that have nearly circular orbits and spiral in (or out) because of the drag forces.

If the angular velocities of grains are larger than that of gas, the grains experience head wind and lose angular momentum to move inward. Inward migration of a grain subject to gas drag, but no radiation pressure or the PR drag, was discussed by Adachi, Hayashi, & Nakazawa (1976) and Weidenschilling (1977). Exposure of dust grains to the radiation pressure often causes the orbital speed of grains to be slower than that of gas. In this case which we study below, the back-wind gives the grains angular momentum so that grains move outward. Below, we study several regimes of migration allowing analytical solutions of the equations of motion.

3.1. Strongly Coupled Case ($T_s \ll 1$)

Consider the limiting case $T_s \ll 1$, in which the stopping time t_s is much smaller than the dynamical timescale Ω_K^{-1}. As will be clear from the results, the particle moves azimuthally at nearly the gas velocity, so that $v_\theta \approx v_g$. The grain assumes a finite terminal radial velocity v_r when the radial forces come into balance so that $dv_r/dt = 0$. The terminal velocity follows from equation (13),

$$v_g^2 - v_K^2\left[1 - \beta\left(1 - \frac{2v_r}{c}\right)\right] - \frac{v_K v_r}{T_s} = 0 \, . \tag{16}$$

The term $2v_r/c$ is negligible. From equations (9) and (11), the above equation becomes

$$v_K(\beta - \eta) - \frac{1}{T_{ss}}\left(1 + \frac{v_r^2}{v_T^2}\right)^{1/2} v_r = 0 \, . \tag{17}$$

Solving this equation, we obtain

$$v_r = \text{sgn}\,(\beta - \eta)\,\frac{v_T}{\sqrt{2}}$$

$$\times \left(\left\{ 1 + \left[2T_{ss}(\beta - \eta)\,\frac{v_K}{v_T} \right]^2 \right\}^{1/2} - 1 \right)^{1/2}. \quad (18)$$

The particle migrates inward if $\beta < \eta$, or outward if $\beta > \eta$.

The velocity of the grain in the azimuthal direction v_θ is almost equal to the gas velocity v_g, but there is a slight difference between these velocities, $\Delta v_\theta = v_\theta - v_g$. The angular momentum of the grain is approximated by $H = mrv_g$. The radial motion changes the angular momentum secularly at a rate

$$\frac{dH}{dt} = \frac{mv_g v_r}{2} \left(1 - \frac{r}{1-\eta}\frac{d\eta}{dr} \right). \quad (19)$$

The torque due to the gas and PR drag forces equals

$$\frac{dH}{dt} = -\frac{m}{T_{ss}} \left(1 + \frac{v_r^2 + \Delta v_\theta^2}{v_T^2} \right)^{1/2} v_K \Delta v_\theta - m\beta_c v_K v_g, \quad (20)$$

where $\beta_c = \beta v_K/c$. As seen from equation (21) below, $\Delta v_\theta \ll v_r$. Thus, Δv_θ^2 in the parenthesis in the above equation can be neglected. Equating the above two expressions for angular momentum change and solving for Δv_θ, the azimuthal wind velocity becomes

$$\Delta v_\theta = -T_{ss}\left(1 + \frac{v_r^2}{v_T^2} \right)^{-1/2} \left[\frac{v_r}{2v_K}\left(1 - \frac{r}{1-\eta}\frac{d\eta}{dr} \right) + \beta_c \right] v_g, \quad (21)$$

where v_r is given by equation (18). Notice that the formulae in this subsection remain valid in the supersonic migration regime, such as might arise from tight coupling of dust grain to gas, but even stronger coupling with stellar radiation field.

3.2. Weakly Coupled Case ($T_s \gg 1$)

If $\beta > 1$ and $T_s \gg 1$, grains are blown away quickly by strong radiation pressure force. In the case of $\beta \gg 1$, only the radiation pressure dominates the grains' dynamics. The grains accelerate their radial velocities with little change in their angular momentum until their radial velocities become so large that the radial gas drag becomes effective to balance with the radiation pressure. The radial motion of grains of $\beta \gg 1$ was discussed by Lecavelier des Etangs, Vidal-Madjar, & Ferlet (1998). In this subsection, we consider the motion of a grain with $\beta < 1$. The grain rotates with the speed $v_\theta = v_K(1-\beta)^{1/2}$ and angular momentum $H = mrv_K(1-\beta)^{1/2}$. The velocity difference from the gas is $\Delta v_\theta = v_K[(1-\beta)^{1/2} - (1-\eta)^{1/2}]$. The torque by the gas drag and PR drag forces is

$$\frac{dH}{dt} = -\frac{m}{T_{ss}}\left(1 + \frac{v_r^2 + \Delta v_\theta^2}{v_T^2} \right)^{1/2} v_K \Delta v_\theta - m\beta_c v_K v_\theta. \quad (22)$$

Because $v_r \ll \Delta v_\theta$ (see eq. [23] below), v_r^2 in the right hand side is neglected. The torque causes radial migration with velocity

$$v_r = \frac{2}{T_{ss}}\left(1 + \frac{\Delta v_\theta^2}{v_T^2} \right)^{1/2}\left[\left(\frac{1-\eta}{1-\beta} \right)^{1/2} - 1 \right]v_K - 2\beta_c v_K. \quad (23)$$

If PR drag force is negligible (the second term in eq. [23] is neglected), a grain of $\beta < \eta$ migrates inward, and a grain of $\beta > \eta$ migrates outward.

3.3. Connecting Formulae For Arbitrary Stopping Time

If the motions of grains and gas are close to the Keplerian circular motion, we can derive approximate formulae connecting the two regimes of weak and strong coupling of grains with gas. In this subsection, we assume that η, $\Delta v_\theta/v_K$, v_r/v_K, and $\beta_c = \beta v_K/c$ are much smaller than unity. Based on the assumption that grains undergo a steady state migration in a disk without executing large radial motions in one turn of the orbit, we replace the full-time derivatives d/dt in the equations of motion (13) and (14) with the advective terms $v_r\,\partial/\partial r$. In other words, we set $\partial/\partial t = 0$. Then, neglecting the second order terms of η, $\Delta v_\theta/v_K$, v_r/v_K, and β_c, the azimuthal equation (14) becomes

$$\Delta v_\theta = -T_s\left(\frac{v_r}{2} + \beta_c v_K \right). \quad (24)$$

Radial equation (13) becomes

$$v_K(\beta - \eta) + 2\Delta v_\theta - \frac{1}{T_s}v_r = 0. \quad (25)$$

Substituting equation (24) into equation (25), we obtain

$$v_r = \frac{\beta - \eta - 2\beta_c T_s}{T_s + T_s^{-1}}v_K. \quad (26)$$

Note that the stopping time T_s defined by equation (9) is a function of v_r and Δv_θ. Thus, v_r and Δv_θ cannot be expressed analytically. If the velocity difference of a grain with respect to gas is subsonic, $T_s \approx T_{ss}$ is independent of the velocity of the grain. In this case, v_r and Δv_θ can be calculated analytically by replacing T_s by T_{ss} in equations (24) and (26). In the supersonic regime, v_r and Δv_θ must be found numerically by an iterative correction method.

3.4. Steady Orbits of Grains

At some distance from the central star, the grain may have a steady circular orbit without radial migration or any torque. On such an orbit, $dv_r/dt = v_r = 0$ and $dv_\theta/dt = 0$. From the r component of equation of motion (13), the azimuthal velocity of the grain is $v_\theta = v_K(1-\beta)^{1/2}$. From the θ-component of equation of motion (14),

$$(v_\theta - v_g) + \beta_c T_s v_\theta = 0. \quad (27)$$

The radius of the steady orbit is calculated as a solution of equation (27) for a given size of a grain s (or β). If PR drag force is negligible ($\beta_c T_s \ll 1$), equation (27) yields corotation with gas, i.e., $v_\theta = v_g$, and consequently

$$\beta = \eta. \quad (28)$$

Thus, a grain has the steady circular orbit at such a distance r from the star, where $\beta = \eta(r)$.

3.5. Size Dependence of Dust Particle Velocity

In a gas disk, small grains of $\beta > \eta$ circulate faster than the gas and migrate outward, while large grains of $\beta < \eta$ rotate slower than gas and migrate inward, if PR drag force is negligible. Figure 2 shows the dependence of the velocity of grains on their sizes. In this figure, $\rho_g = 2.18 \times 10^{-17}$ g
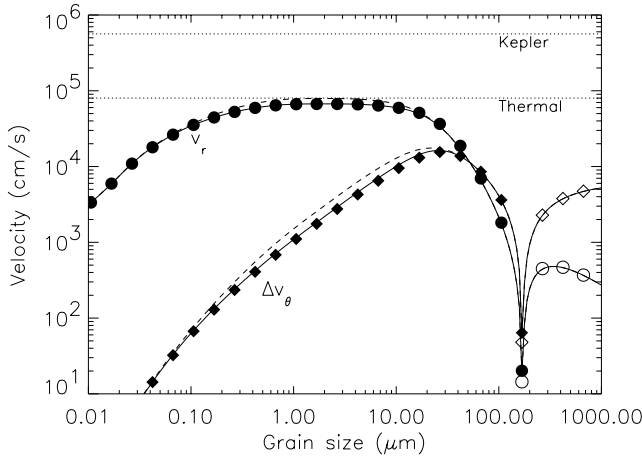
FIG. 2.—Velocities of dust grains at 70 AU in the gas disk of model 1 described in § 4. The circles show the radial velocities v_r and the diamonds show the relative velocities in the azimuthal direction between the grains and gas, $\Delta v_\theta = v_\theta - v_g$. Filled symbols represent positive v_r and negative Δv_θ (outward migration) and open symbols represent negative v_r and positive Δv_θ (inward migration). The solid lines show the approximate formulae (24) and (26) calculated numerically after the iterations for the supersonic correction. The dashed lines show the first guesses of iteration, which are calculated using the subsonic stopping time T_{ss} instead of T_s. The horizontal dotted lines show the Kepler and mean thermal velocities $(3v_T/4)$ at 70 AU in the model 1 disk.

cm^{-3}, $v_T = 1.07 \times 10^5$ cm s^{-1}, and $\eta = 2.24 \times 10^{-2}$. These are the values the disk in model 1, described below in § 4.1, has at 70 AU. The radial velocities v_r are shown by circles. The filled circles represent that grains move outward ($v_r > 0$), while open circles represent that grains move inward ($v_r < 0$). These symbols are plotted by monitoring the velocities of grains in the numerical calculations of their orbits, described in § 5. The grains smaller than 174 μm migrate outward, while larger grains migrate inward. The velocity differences Δv_θ in the azimuthal direction between grains and gas are shown by diamonds. The grains smaller than 174 μm rotate faster than gas, while larger grains rotate slower. The 174 μm grains have $\beta = \eta$, and thus steady circular orbits without radial migration.

The grains with the size $0.1 \lesssim s \lesssim 10$ μm have similar values of the radial velocity. These grains' β are much larger than η and inversely proportional to the grain size s (see Fig. 1). The stopping time of these grains are much smaller than the orbital period ($T_s = 1$ at $s \approx 30$ μm) and proportional to s (eq. [10]). It is seen that the radial velocity is constant in this size range, following from equation (26).

The solid lines show the approximate formulae (24) and (26). The plotted values were obtained numerically after several iterations for the supersonic correction. The dashed lines show the first guesses of iteration, which are calculated using the subsonic stopping time T_{ss} instead of T_s. The deviations between the approximate and exact formulae for the $0.1 \lesssim s \lesssim 10$ μm grains are due to the fact that their radial velocities are comparable to the thermal speed of gas.

4. SEGREGATION OF DUST ACCORDING TO SIZE

As shown in § 3, dust grains migrate inward or outward until they feel no net torque. The radius of the steady orbit is the function of grain's size s, which is obtained as the solution of equation (27). Thus, in a gas disk, grains segre-

gate according to their sizes. In this section, we investigate the segregation of grains in a disk with fixed gas profile.[3]

4.1. Models of Gas Disks

We assume that the temperature and density structures of the gas disk have power-law forms. The temperature structure of the disk that is transparent to the central star's visible radiation is (Hayashi 1981)

$$T = 278\left(\frac{L}{L_\odot}\right)^{1/4}\left(\frac{r}{1\ \mathrm{AU}}\right)^q \mathrm{K} ,\qquad (29)$$

where power-law index $q = -\frac{1}{2}$. The mid-plane density also has a power law, and at the outer radius of the disk r_{out}, the disk has an edge of characteristic width Δr_{out}. The density structure is modeled by

$$\rho_g = \rho_0\left(\frac{r}{1\ \mathrm{AU}}\right)^p \frac{1}{2}\left(\tanh\frac{r_{out} - r}{\Delta r_{out}} + 1\right).\qquad (30)$$

The width of the edge Δr_{out} should be determined by the physical process of the disk truncation, e.g., the photoevaporation or the tidal truncation by binary companions. While we have no detailed knowledge of the disk edge, the dynamics of gas disks constrains the lower limit of Δr_{out}. If the edge is too narrow, the steep pressure gradient at the edge changes the radial velocity profile of gas so much that the specific angular momentum of gas decreases with the radius, which leads to Rayleigh instability. Hence, Δr_{out} must be larger than about the disk scale height, i.e., if $\Delta r_{out} = C_{out}(c_s/\Omega_K)r_{out}$, then C_{out} should be larger than unity. The sound and thermal velocity c_s and v_T are, respectively,

$$c_s = \left(\frac{\Gamma kT}{\mu_g m_H}\right)^{1/2}$$

$$= 1.17 \times 10^5\left[\frac{\Gamma}{1.4}\frac{2.34}{\mu_g}\left(\frac{L}{L_\odot}\right)^{1/4}\right]^{1/2}\left(\frac{r}{1\ \mathrm{AU}}\right)^{q/2} \mathrm{cm\ s}^{-1} ,$$

$$v_T = \frac{4}{3}\left(\frac{8kT}{\pi\mu_g m_H}\right)^{1/2}$$

$$= 2.11 \times 10^5\left[\frac{2.34}{\mu_g}\left(\frac{L}{L_\odot}\right)^{1/4}\right]^{1/2}\left(\frac{r}{1\ \mathrm{AU}}\right)^{q/2} \mathrm{cm\ s}^{-1} ,\quad (32)$$

where Γ is the adiabatic exponent. The ratio of the pressure gradient force to the gravitational force η is (eq. [12])

$$\eta = -\left(\frac{c_s}{r\Omega_K}\right)^2\frac{1}{\Gamma}\left[p + q - \frac{r\ \mathrm{sech}^2 x}{\Delta r_{out}(\tanh x + 1)}\right],\quad (33)$$

where $x = (r_{out} - r)/\Delta r_{out}$.

In model 1, we adopt following assumptions. The disk gas consists of molecular hydrogen and atomic helium ($\mu_g = 2.34$ and $\Gamma = 1.4$). The central star has the mass and luminosity of HR 4796A: $M = 2.5\ M_\odot$ and $L = 21.0\ L_\odot$, respectively. The power-law indexes of the density and temperature are $p = -2.25$ [which corresponds to the power-law index of surface density, $p_s = p + (q + 3)/2 = -1.0$]

---

[3] Gas profile will change significantly in time if the total gas mass is much smaller than the dust mass, a case which we do not consider here. Gas migration and dust migration have opposite directions and magnitudes following from the conservation of total angular momentum.

TABLE 1

MODEL PARAMETERS

Model	Star	M_g ($M_\oplus$)	r_{out} (AU)	p	C_{out}	K	M_d ($M_\oplus$)	L_d/L
1......	HR 4796A	10	100	−2.25	1.05	1×10^{-9}	0.90	1.7×10^{-2}
2......	...	1	...	...	...	...	0.10	2.0×10^{-3}
3......	...	...	...	−2.75	...	...	0.37	8.2×10^{-3}
4......	...	...	...	−1.25	...	...	3.10	4.2×10^{-2}
5......	...	...	...	...	2.0	...	0.72	1.4×10^{-2}
6......	...	...	...	...	...	2×10^{-8}	0.05	9.1×10^{-4}
7......	...	4	80	...	...	...	0.31	8.2×10^{-3}
8......	HD 141569A	50	370	...	...	...	4.23	1.1×10^{-2}

NOTE.—Ellipses mean that the same value as model 1 is used. See § 6.1 for the definition of K and § 7.1 for M_d and L_d.

and $q = -1/2$, respectively. The outer radius of the gas disk is $r_{out} = 100$ AU. The width of the edge of gas disk, $\Delta r_{out} = C_{out}(c_s/\Omega_K)r_{out}$, must be larger than the disk scale height. We adopt $C_{out} = 1.05$, which yields $\Delta r_{out} = 12.1$ AU. The mass

of the gas disk is $M_g = 10\ M_\oplus$, which corresponds to $\rho_0 = 3.12 \times 10^{-13}$ g cm^{-3}. The dust grains have material density of $\rho_d = 1.25$ g cm^{-3}. We also consider the other models of the gas disk: smaller gas mass ($M_g = 1\ M_\oplus$; model 2), steeper and gentler density gradient ($p = -2.75$, $p_s = -1.5$; model 3, and $p = -1.25$, $p_s = 0$; model 4), and wider edge of the disk ($C_{out} = 2.0$; model 5). The values of model parameters are summarized in Table 1.

4.2. Segregation of Grains

Figure 3 shows the ratio of pressure gradient force to the gravitational force η as a function of radius r. The solid line shows η for model 1. For comparison, η of the gas disk with a wider edge (model 5) is shown as the dashed line. The value of the gas mass does not affect η and model 2 ($M_g = 1\ M_\oplus$) has the same profile of η as that in model 1. The profiles of η in model 3 and 4 (different density gradient; $p = -2.75$ and -1.25) are similar to that in model 1. In model 1 (solid line), η increases gradually with radius to 80 AU, and then more rapidly at the edge of the disk around 100 AU, because of the steep decrease in the gas density and pressure there. A wider disk edge (cf. the dashed line) causes a more gradual rise of η.

The radius of the steady orbits of grains are calculated from equation (27) and are plotted in Figure 4 (we plot the grain size s as a function of radius r). In our models, the PR drag force is negligible compared to the gas drag force except when the grains are at the outside of the disk, $r \gtrsim 130$ AU. The dotted line shows the case in which the PR drag force is not included in model 1 and coincides with solid line for $r \lesssim 130$ AU. Thus, the PR drag force can be neglected and the grains segregate to satisfy $\beta = \eta$. The smaller grains stay at farther from the central star. At the edge of the disk where η varies rapidly ($80 \lesssim r \lesssim 110$ AU), grains in the size range $10 \lesssim s \lesssim 100\ \mu$m find stable orbits and concentrate there. Again, a wider edge in model 5 (dashed line) gives rise to a milder concentration of grains.

5. ORBITAL EVOLUTION OF DUST GRAINS

In § 3 we derived the radial velocities of grains analytically assuming the orbits of the grains are nearly circular. In this section, we calculate the orbital evolution of the grains numerically by integrating the equations of motion (13) and (14). It will be shown that the grains migrate to settle down in their own steady circular orbits, except at the outer edge of the gas disk, where the eccentricities of the grains' orbits are pumped up and dust disk extends beyond the gas disk.
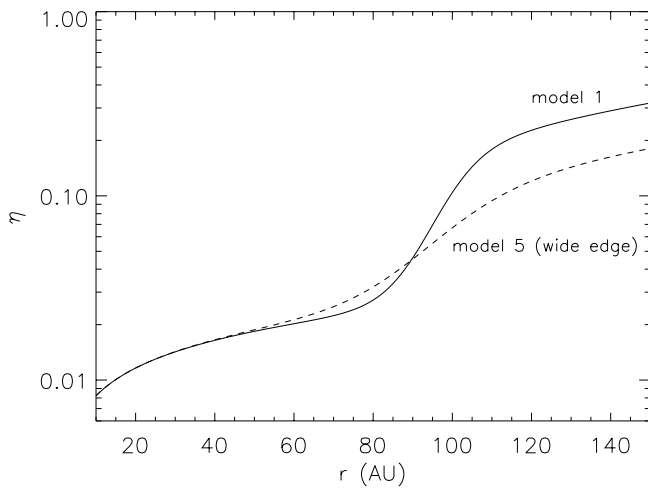

FIG. 3.—Ratio of gas pressure force to gravity, η, in the disk of model 1 (solid line) and model 5 (dashed line). The disk in model 5 has a wider edge at 100 AU than that in model 1.
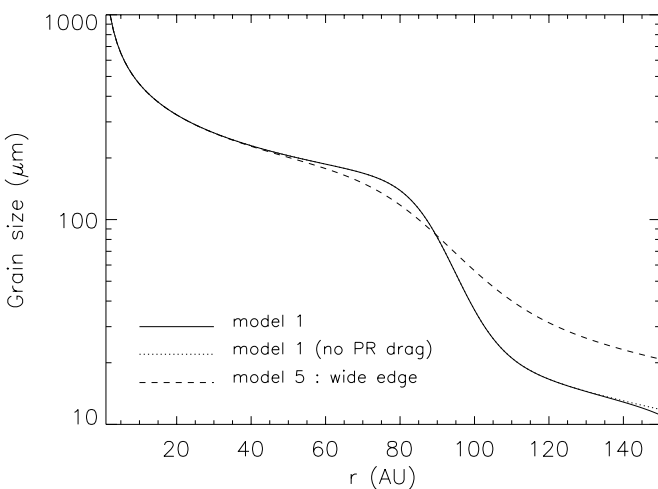

FIG. 4.—Size of grains on steady orbits with radii r. The solid and dashed lines show the grain size in model 1 and in model 5, respectively. The dotted line represents the case where the Poynting-Robertson (PR) drag is neglected in model 1, and is different from the solid line (including the PR drag) only for $r \gtrsim 130$ AU.
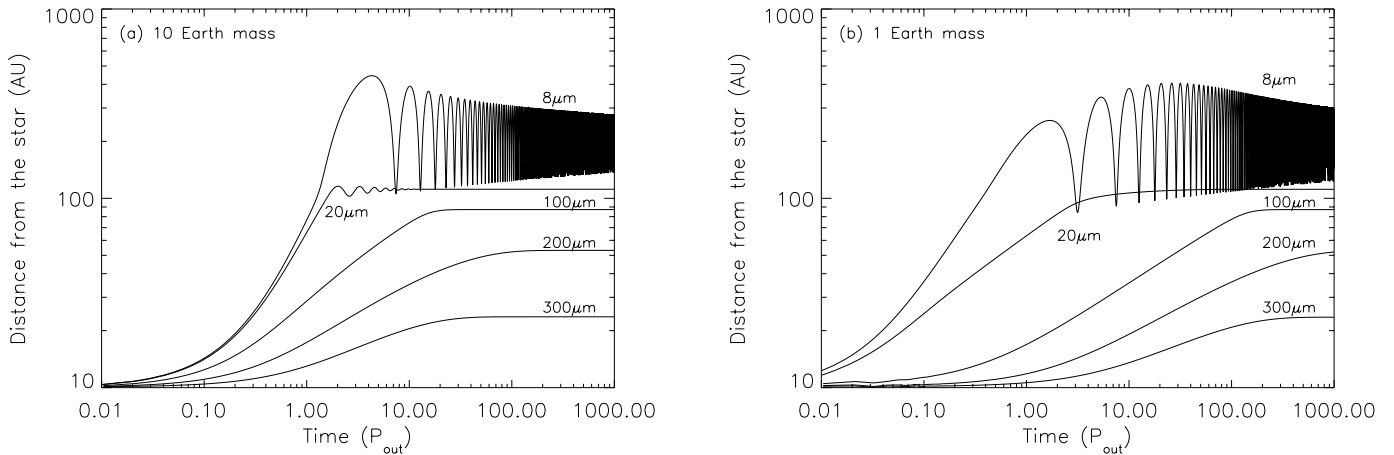
FIG. 5.—(a) Evolution of the orbital radii r of 8–300 μm grains in the disk of model 1. The mass of the gas disk is 10 $M_\oplus$. The time is measured by the orbital period at 100 AU, $P_{\rm out} = 632$ yr. The grains are generated at 10 AU and move outward until arriving at the steady orbits. The oscillations of r of 8 μm and 20 μm grains are due to the excitation of their orbital eccentricities at the edge of the gas disk. (b) The same as Fig. 5a, but for model 2 where the gas disk is 1 $M_\oplus$.

5.1. Orbital Evolution and Radial Distribution of Grains

In Vega-type and transitional disks, dust grains are produced as ejecta of collisions between much larger parent bodies such as planetesimals, comets, or meteorites. These parent bodies are not affected by radiation pressure and have Keplerian orbits. If the velocity of ejection is much smaller than the orbital speed, the grains produced by collisions have the same Keplerian velocities as their parent bodies have. Because grains experience radiation pressure, the velocities of the grains are larger than that the grain on the circular orbit would have. Thus, the grains are endowed with orbital eccentricities $e \approx \beta/(1 - \beta)$ (the equality becoming exact, if parent orbits are circular). However, if the density of gas is high enough that the stopping time is much smaller than the orbital period, the eccentricities of grains decrease quickly by the gas drag force and grains' orbits are circularized. In the inner part of our model disks ($r \lesssim 20$ AU), the orbits of grains with size $s \lesssim 100$ μm are circularized rapidly ($T_{\rm ss} < 1$). Then, the grains spiral in or out as discussed in § 3.

Figure 5 shows the evolution of the distance of grains from the central star, r. The grains are assumed to be produced at 10 AU with eccentricity $e = \beta/(1 - \beta)$. These initial values are not important because the grains rapidly forget their initial states due to the gas drag force. The orbits of the grains are calculated by integrating the equations of motion (13) and (14) numerically by seventh-order Runge-Kutta method. The integration are performed until $t = 1000P_{\rm out}$, where $P_{\rm out} = 2\pi/\Omega_{\rm K}(r_{\rm out}) = 632$ yr is the orbital period at $r_{\rm out}(= 100$ AU). Figure 5a shows the evolution of orbits in model 1. The orbits of the grains are quickly circularized and the grains migrate outward. The grains larger than 100 μm arrive at their steady orbits in $\sim 100P_{\rm out}$, and settle down in these orbits. Smaller grains migrate to farther locations. A grain of 20 μm arrives at the radius of the steady orbit that is in the outer edge of the disk in $1P_{\rm out}$, then its orbital eccentricity is pumped up. The excitation of the eccentricity is seen in Figure 5a as the oscillation of the distance r. Finally, the orbital eccentricity of the 20 μm grain decreases owing to the gas drag force, and the grain stays in the circular steady orbit. The orbital eccentricity of a grain of 8 μm is also pumped up when the grain arrives at

the edge of the disk, and then decreases. Because the 8 μm grain spends most of its time staying outside the disk (it is in the gas disk only when being just around the pericenter of the orbit), however, the gas drag force is not strong enough to damp the eccentricity quickly. Thus, the 8 μm grain stays in eccentric orbit for long time (more than $1000P_{\rm out}$). The evolution of orbits in the disk with smaller gas mass ($M_g = 1$ $M_\oplus$; model 2) is shown in Figure 5b. The main feature of the evolution is similar to that in model 1. The settling time for grains to arrive at the steady orbits is longer than that in model 1; $\sim 100P_{\rm out}$ for 100 and 300 μm grains and $\sim 1000P_{\rm out}$ for 200 μm grains.

Figure 6 shows the positions of the pericenter and apocenter at $t = 1000P_{\rm out}$ against the grain size. The solid line corresponds to model 1. The grains smaller than 6.7 μm are blown away (launched into hyperbolic orbits when they move to the outer edge of the gas disk). The grains of $6.7 \leq s \leq 12$ μm have eccentric orbits ($e > 0.01$) with their pericenters on the outer edge of the gas disk. These grains
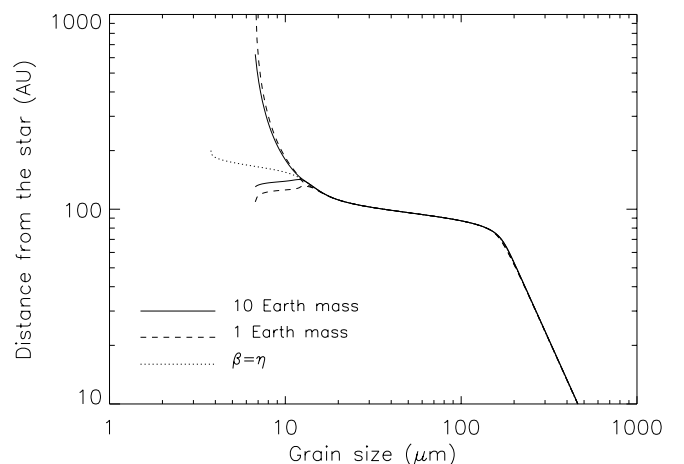

FIG. 6.—Apocenter and pericenter distances of the grain orbits. The grains are generated at 10 AU and the orbits at $t = 1000P_{\rm out}$ are shown by the solid line (in the gas disk with 10 $M_\oplus$; model 1) and dashed line (in the gas disk with 1 $M_\oplus$; model 2). The orbits of grains larger than about 10 μm are circular and the distances of the apocenter and pericenter coincide with the value derived by the condition $\beta = \eta$ (dotted line).

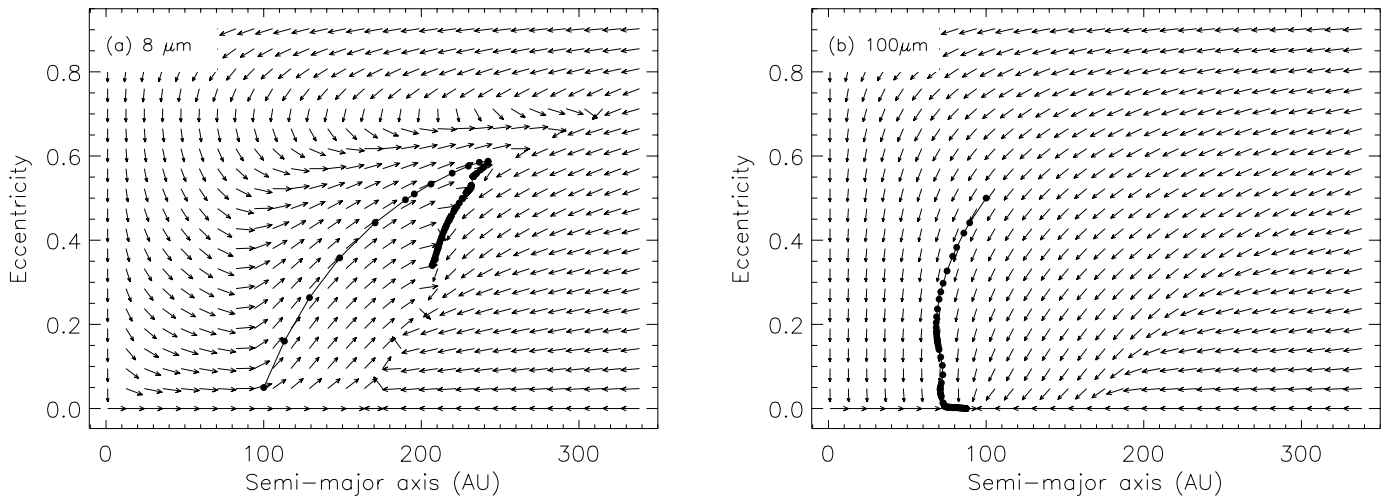FIG. 7.—Evolution of the orbital elements of (a) an 8 μm grain and (b) a 100 μm grain. The gas disk is that of model 1. Arrows show the directions of the orbital evolution obtained by the perturbation equations (Gauss's equations). The length of arrows is constant and does not represent the rate of evolution. The circles show the evolution of orbital elements of test particles, which are obtained directly from the orbital calculations. The initial values of the test particles' orbital elements are (a) $a = 100$ AU and $e = 0.05$ and (b) $a = 100$ AU and $e = 0.5$. The circles are plotted until $t = 1000P_{out}$ using logarithmic time intervals: the first one is $0.01P_{out}$ and each next time interval is 1.2 times the previous one.

make dust disk extended outside the gas disk. The grains larger than 12 μm have circular orbits. The radii of the circular orbits coincide to the radii calculated from the condition that the orbits are steady (eq. [27]) and shown by the dotted line. The dashed line corresponds to model 2 (smaller gas mass; $M_g = 1 M_\oplus$). Because the gas drag force is smaller than that in model 1, the eccentricities of small grains remain larger (see § 5.2 below). The size of the smallest grain having circular orbit is 13 μm, slightly larger than that in model 1.

5.2. Excitation of Eccentricity at the Disk's Outer Edge

The orbital eccentricities of grains smaller than 20 μm are excited when these grains arrive at the outer edge of the gas disk. These grains have large β (0.19 for 20 μm and 0.47 for 8 μm grains). Until the grains arrive at the disk edge, the gas drag force on such the small grains are strong enough that the grains are trapped by the gas and move with the gas. The gas rotates faster than the grains ($\eta = 0.10$ at r_{out}), and the grains gain angular momentum from the gas and move outward. Because the gas density decreases rapidly at the disk edge, the gas drag force ceases suddenly when the grains pass through the disk edge. Therefore, the grains are launched into the Kepler orbit (modified by the radiation pressure) with initial velocity of $v_g = [0, v_K(1 - \eta)^{1/2}]$ at the disk edge. With this initial velocity, the orbits of the grains are eccentric with $e = (\beta - \eta)/(1 - \beta)$ and pericenters at the disk edge. After launching into the eccentric orbits, the grains experience the gas drag force that works to circularize the grains' orbits only when they are around their pericenter at the disk edge. Thus, the eccentricities of the grains decreases slowly.

In the above discussion, we assumed that the gas density in the disk is high enough for the gas drag force to hold the grains tightly with the gas. We arrive at the same conclusion when the gas density is low and the gas drag force is not strong enough to hold the grains. Consider a small grain the β of which is much larger than η at the disk edge, and assume that the grain has slightly eccentric orbit. The semi-major axis and eccentricity of its orbit are a and e, respec-

tively. Because $\beta \gg \eta$, the grain rotates much slower than the gas and experiences back-wind throughout its orbit, even when it is at the pericenter. The evolution of the eccentricity of the orbit by the perturbating drag force is given by the Gauss's equation (Brouwer & Clemence 1961)

$$\frac{de}{dt} = \frac{1}{v_K(a)} \left(\frac{1 - e^2}{1 - \beta}\right)^{1/2}$$

$$\times \left[F_r \sin \psi + F_\psi \left(\frac{\cos \psi + e}{1 + e \cos \psi} + \cos \psi\right)\right], \quad (34)$$

where ψ is a true anomaly, and F_r and F_ψ are the radial and azimuthal components of gas drag force, respectively. At the pericenter ($\psi = 0$) and the apocenter ($\psi = \pi$), equation (34) becomes

$$\frac{de}{dt} = \pm \frac{2}{v_K(a)} \left(\frac{1 - e^2}{1 - \beta}\right)^{1/2} F_\psi, \quad (35)$$

where plus and minus signs correspond to the pericenter and apocenter, respectively. The grain experiences back-wind throughout the orbit. Thus, F_ψ is positive both at the pericenter and apocenter. From the equation (35), it is seen that the eccentricity increases at the pericenter and decreases at the apocenter. When the grain is in the edge of the disk, the gas density at the pericenter is much higher than that at the apocenter. Therefore, the grain experiences stronger back-wind at the pericenter and its eccentricity increases. The increase in the eccentricity accompanies the increase in the velocity at the pericenter and continues until the velocity arrives at the same velocity of the gas. When velocity of the grain at the pericenter becomes the same as that of the gas, the eccentricity has grown up to be $e = (\beta - \eta)/(1 - \beta)$. After the eccentricity arrives at the maximum value, it starts to decrease. This is because the gas drag force at the pericenter pushes the position of the pericenter slightly outward. The eccentricity evolves to keep the velocity of the grain at the pericenter being equal to the velocity of the gas and maintains the value of $e = (\beta - \eta)/(1 - \beta)$. Because η is an increasing function of r, the value of η at the pericenter increases as the pericenter moves

outward, and the eccentricity decreases. The gas density at the pericenter and the gas drag force decrease as the pericenter moves outward, and the speed of the eccentricity damping becomes more slowly.

Figure 7a illustrates the evolution of the eccentricity and the semimajor axis of an 8 μm grain. The average of the change in the eccentricity over one orbital period P is calculated by

$$\left\langle \frac{de}{dt} \right\rangle = \frac{1}{P} \int_0^P \frac{de}{dt} \, dt \, . \tag{36}$$

The integration is performed numerically and the effect of the PR drag force is included. The Gauss's equation of the variation in the semimajor axis is

$$\frac{da}{dt} = \frac{2}{\Omega_K(a)(1 - \beta)^{1/2}(1 - e^2)^{1/2}}$$
$$\times \left[F_r e \sin \psi + F_\psi \frac{a(1 - e^2)}{r} \right] . \tag{37}$$

The average over one orbital period, $\langle da/dt \rangle$, is calculated in analogy with equation (36). The evolutions of a and e are shown in Figure 7a as arrows. The length of the arrows are set to be constant and does not represent the rate of the variation. A grain inside the disk ($a \lesssim 100$ AU) moves outward and its eccentricity decreases. If the grain's pericenter is on the edge of the gas disk ($100 \lesssim a \lesssim 200$ AU and $0 < e \lesssim 0.6$), its eccentricity grows. For a grain of which the pericenter is outside the disk, the eccentricity and semimajor axis decrease. The evolution of the orbit of a grain the initial a and e of which are 100 AU and 0.05, respectively, is plotted as circles on Figure 7a. The time interval of plotting circles is logarithmic: the first time interval is $0.01P_{out}$ and each time interval is 1.2 times the previous one. The last circle represents the orbit at $t = 1000P_{out}$. First, the grain's semimajor axis and eccentricity grow, then the eccentricity turns to decrease.

In Figure 7b, the evolution of orbital elements of a 100 μm grain is shown for comparison. It is seen that the eccentricity always decreases and the semimajor axis changes toward the value of the steady orbit. Circles show the evolutional path of a grain with the initial semimajor axis $a = 100$ AU and eccentricity $e = 0.5$. The eccentricity decreases quickly, and the semimajor axis decreases at first, and then increases as the grain approaches the steady orbit.

6. LIFETIME AND DENSITY OF DUST GRAINS

The grains larger than about 10 μm have steady circular orbits in the gas disk, as shown in Figure 6. The size of grains in the steady orbit is a function of distance from the star r, written as

$$s_s = s_s(r) \, . \tag{38}$$

The grains of size s_s in the steady orbit do not collide with each other, because their orbits are circular.

However, smaller grains ($s < s_s$) the steady orbits of which are farther from the star flow outward and cross the orbit of grains of size s_s. These smaller grains collide with and destroy the grains in the steady orbit. In this section, we calculate the lifetime of grains in the steady circular orbit in the gas disk, then estimate their number density. The small grains ($s \lesssim 10$ μm) extended outside the gas disk have

eccentric orbits and collide with each other. The calculation of the lifetime of these small grains remains as future work.

The grains are originally produced by collisions of parent bodies such as planetesimals or comets. In this section, we assume that these parent bodies are distributed in the innermost part of the gas disk (say, ~ 10 AU). The grains produced by collisions migrate outward to settle down in the steady orbits. However, the steady orbits can be called parking orbits at best. When the grain on the steady orbit is broken up by collisions, the fragments flow outward again and settle down in the new parking orbits. Thus, grains gradually migrate outward every collisional destructions. The steady orbit of grains of size $10 \lesssim s_s \lesssim 100$ μm are concentrated at the edge of the gas disk (Fig. 6). Thus, it is expected that the grains of $10 \lesssim s_s \lesssim 100$ μm gather in the edge of the gas disk and make a dust ring. The grains are finally blown away when collisional destruction reduces them to sizes so small that they cannot have steady orbit in the gas disk.

6.1. Collisional Destruction of Grains

There are two phases of collisional destruction. A grain is broken up by a collision with large impact kinetic energy (catastrophic disruption), while part of a grain is ejected by a collision with small energy (cratering). Consider the destruction of a grain of mass $m = 4\pi\rho_d s^3/3$ by the collision with a grain of mass m'. The mass Δm lost from the target grain m by cratering with the collisional velocity u is (Holsapple 1993)

$$\frac{\Delta m}{m} = K \frac{m'}{m} \left(\frac{u}{\mathrm{cm\ s^{-1}}} \right)^{3\mu} , \tag{39}$$

where K is a coefficient representing efficiency of cratering and the value of the exponent μ is uncertain now. We assume that the mass loss Δm is proportional to the impact energy and adopt $\mu = \frac{2}{3}$. In equation (39), $\Delta m/m$ becomes larger than 1 for large u, that corresponds to catastrophic disruption. Of course, $\Delta m/m$ cannot be larger than 1 and should be

$$\frac{\Delta m}{m} = \max \left\{ K \frac{m'}{m} \left(\frac{u}{\mathrm{cm\ s^{-1}}} \right)^2, 1 \right\} . \tag{40}$$

The value of K is calculated from the minimum energy for the catastrophic disruption. Let Q^* be the threshold of the specific energy per unit target mass for the catastrophic disruption. The threshold energy Q^* depends on the impact velocity u and target size s, and written as (Housen & Holsapple 1999)

$$Q^* = Q_0^* \left(\frac{u}{\mathrm{km\ s^{-1}}} \right)^{2 - 3\mu} \left(\frac{s}{10\ \mathrm{cm}} \right)^\delta = Q_0^* \left(\frac{s}{10\ \mathrm{cm}} \right)^\delta , \tag{41}$$

where we used $\mu = \frac{2}{3}$. The values of Q_0^* are obtained by the experiments: $Q_0^* = 10^7$ ergs g^{-1} for rocks (Housen & Holsapple 1999) and $Q_0^* = 4 \times 10^5$ ergs g^{-1} for ice (Fig. 9 in Arakawa 1999). The value of the exponent δ is uncertain. Housen & Holsapple (1990) proposed that $\delta = -0.24$, and Housen & Holsapple (1999) recommended that $\delta = -0.67$. We are interested in the lifetime and density of grains constituting the dust ring at the edge of the gas disk. The sizes of these grains are $10 \lesssim s \lesssim 100$ μm. Thus, we estimate Q^*
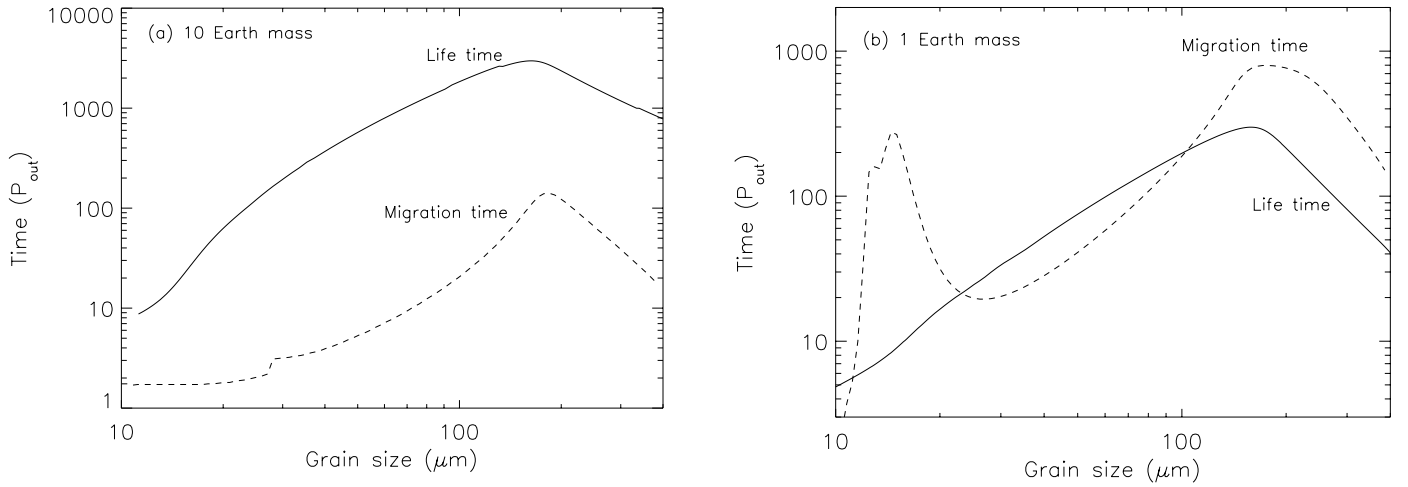
FIG. 8.—Life and migration time of dust grains. The solid line shows the lifetime of grains on steady orbits under the collisional destruction. The dashed line shows the migration time from 10 AU to the 99% of the steady orbit radius. (a) The gas mass is $M_g = 10 \, M_\oplus$ (model 1). (b) $M_g = 1 \, M_\oplus$ (model 2).

for the grain of size $s = 50 \, \mu m$ as

$$Q^* = \begin{cases} 6.2 \times 10^7 - 1.6 \times 10^9 \text{ ergs g}^{-1} & \text{for rocks,} \\ 2.5 \times 10^6 - 6.5 \times 10^7 \text{ ergs g}^{-1} & \text{for ice,} \end{cases} \quad (42)$$

where smaller values correspond to $\delta = -0.24$ and larger values correspond to $\delta = -0.67$. The definition of the catastrophic disruption is $\Delta m/m \geq \frac{1}{2}$, which yields

$$K = \frac{1}{4Q^*} = \begin{cases} 1.5 \times 10^{-10} - 4.0 \times 10^{-9} & \text{for rocks,} \\ 3.8 \times 10^{-9} - 1.0 \times 10^{-7} & \text{for ice.} \end{cases} \quad (43)$$

6.2. Lifetime of Grains

In this subsection, we derive the equation for the lifetime of a grain of size s_s on the steady orbit. A grain s_s collide with smaller grains crossing its orbit. The probability of collision with grains in the size range $[s', s' + ds']$ in 1 s is

$$p_{col} = \sigma u n' ds' , \quad (44)$$

where $\sigma = \pi (s_s + s')^2$ is the collisional cross section, $n' ds'$ is the number density of grains in the size range $[s', s' + ds']$, and $u = |v' - v|$ is the relative velocity of the grains. The velocity of the grain s_s is the same as the velocity of the gas, i.e., $v = (0, v_g)$. The velocity $v' = (v_r', v_\theta')$ of the grain s' is obtained by the orbital calculations of grains described in § 5.1. For small grains in the inner part of the disk where the gas density is high, the nondimensional stopping time T_s is much smaller than unity. We use the analytical formulae (18) and (21) to calculate the velocities of small grains if $T_s \ll 1$, because numerical calculations of orbits consume much time. The density $n' ds'$ is calculated from the production rate of dust grains. Let the number of grains that are in the size range $[s', s' + ds']$ and cross the circle of the radius r (the orbit of the grain s_s) in 1 s be $\dot{N}_{pro}(r, s') ds'$. The number density $\dot{N}_{pro}(r, s')$ is assumed to have power-law form in s'. We also assume that the grains are originally produced innermost part of the gas disk and flow outward. Only the grains smaller than s_s cross the orbit of the grain s_s. The grains larger than s_s stay in their steady orbits which are closer to the star, but when they are broken to pieces smaller than s_s, these pieces flow outward and cross the orbit of the grain s_s. Thus, the grains crossing the orbit of

the grain s_s are constituted of smaller grains, and $\dot{N}_{pro}(r, s') ds'$ are written as

$$\dot{N}_{pro}(r, s') ds' = \begin{cases} \dot{N}_0(r) \left(\dfrac{s'}{cm} \right)^\alpha ds' & \text{for } s \leq s_s , \\ 0 & \text{for } s > s_s . \end{cases} \quad (45)$$

The mass of grains crossing the orbit of the grain s_s in 1 s is

$$\dot{M}_{pro} = \int_{s_{min}}^{s_s} \frac{4\pi}{3} s'^3 \rho_d \dot{N}_0 \left(\frac{s'}{cm} \right)^\alpha ds' , \quad (46)$$

where s_{min} is the minimum size of grains. In the steady state, $\dot{M}_{pro}$ is independent on r and represents the mass production rate of grains in the gas disk. From equation (46),

$$\dot{N}_0(r) = \frac{3\dot{M}_{pro}}{4\pi\rho_d} \left[\int_{s_{min}}^{s_s} s'^3 \left(\frac{s'}{cm} \right)^\alpha ds' \right]^{-1} . \quad (47)$$

Note that $\dot{N}_0$ is the function of r because s_s is the function of r. The other expression of number flux is $\dot{N}_{pro}(r, s') ds' = 2\pi r h_d v_r' n' ds'$, where h_d is the thickness of the dust disk. Solving this equation and equation (45) gives

$$n' ds' = \begin{cases} \dfrac{\dot{N}_0}{2\pi r h_d v_r'} \left(\dfrac{s'}{cm} \right)^\alpha ds' & \text{for } s \leq s_s , \\ 0 & \text{for } s > s_s . \end{cases} \quad (48)$$

The mass loss rate from the grain s_s with mass m is

$$\frac{1}{m} \frac{dm}{dt} = \int_{s_{min}}^{s_s} \frac{\Delta m}{m} \sigma u n' ds'$$

$$= \frac{\dot{N}_0}{2} \left(\frac{h_d}{r} \right)^{-1} \int_{s_{min}}^{s_s} \frac{\Delta m}{m} \frac{u}{v_r'} \left(\frac{s_s + s'}{r} \right)^2 \left(\frac{s'}{cm} \right)^\alpha ds' . \quad (49)$$

The lifetime of the grain s_s is

$$t_{life} = m \left(\frac{dm}{dt} \right)^{-1} = 2\dot{N}_0^{-1} \frac{h_d}{r}$$

$$\times \left[\int_{s_{min}}^{s_s} \frac{\Delta m}{m} \frac{u}{v_r'} \left(\frac{s_s + s'}{r} \right)^2 \left(\frac{s'}{cm} \right)^\alpha ds' \right]^{-1} . \quad (50)$$

6.3. *Spatial Density of Grains*

The number density of grains in the steady orbits is determined by the balance between the supply of new grains to the steady orbits and the removal of the grains through the collisional destruction. Consider an annular part of the disk between r and $r + dr$. The annulus is made of the grains of the size $[s_s, s_s + (ds_s/dr)dr]$. The total number of the grains in the annulus is

$$N_s \, ds_s = 2\pi r h_d \, n_s \, dr \; , \qquad (51)$$

where n_s is the number density of the grains in the steady orbits.[4] The number of grains destroyed by collisions in 1 s is

$$\dot{N}_{\rm des} \, ds_s = \frac{N_s \, ds_s}{t_{\rm life}} = \frac{2\pi r h_d \, n_s \, dr}{t_{\rm life}} \; . \qquad (52)$$

The supply of the grains to the annulus is $\dot{N}_{\rm pro}(r, s_s)ds_s = \dot{N}_0(s_s/{\rm cm})^\alpha ds_s$. In the steady state, the rate of destruction and supply balance with each other. From $\dot{N}_{\rm des} \, ds_s = \dot{N}_{\rm pro}(r, s_s)ds_s$, we obtain

$$n_s = \frac{1}{\pi r^2} \left(\frac{s_s}{\rm cm}\right)^\alpha \frac{ds_s}{dr} \left[\int_{s_{\rm min}}^{s_s} \frac{\Delta m}{m} \frac{u}{v_r'} \left(\frac{s_s + s'}{r}\right)^2 \left(\frac{s'}{\rm cm}\right)^\alpha ds'\right]^{-1} . \qquad (53)$$

We define the optical depth of the dust disk in the vertical direction using the geometrical cross section as

$$\tau = \pi s_s^2 h_d \, n_s = \frac{s_s h_d}{r^2} \left(\frac{s_s}{\rm cm}\right)^{\alpha+1} \frac{ds_s}{dr}$$

$$\times \left[\int_{s_{\rm min}}^{s_s} \frac{\Delta m}{m} \frac{u}{v_r'} \left(\frac{s_s + s'}{r}\right)^2 \left(\frac{s'}{\rm cm}\right)^\alpha \frac{ds'}{\rm cm}\right]^{-1} . \qquad (54)$$

Note that the density and optical depth of the grains are independent on $\dot{N}_0$ or the production rate of grains $\dot{M}_{\rm pro}$.

6.4. *Results of Numerical Calculations*

In this subsection, we calculate the lifetime of grains and density (optical depth) of the dust disk in model 1. We assume that the grains are made of rocky material and adopt $K = 1 \times 10^{-9}$. The mass production rate of grains is uncertain. The models of dust disks (however, without gas disks) suggest that the rate of mass loss from the disk is of order $10^{-6} \, M_\oplus \, {\rm yr}^{-1}$ for β Pic (Artymowicz & Clampin 1997), and HR 4796A (Augereau et al. 1999b). In the steady state, the mass-loss rate balances with the mass production rate. We adopt mass production rate $\dot{M}_{\rm pro} = 10^{-6} \, M_\oplus \, {\rm yr}^{-1}$. The density of grains or the optical depth of the disk do not depend on the mass production rate, while the lifetime of grains is inversely proportional to it. The thickness of the dust disk is assumed to be $h_d = 0.1r$ and the minimum size of grains $s_{\rm min} = 0.01 \, \mu$m is adopted. The power-law index of $\dot{N}_{\rm pro}$ in the equation (45) is assumed to be $\alpha = -3.5$, a typical value usually assumed for collisional cascade.

The solid line in Figure 8a shows the lifetime of grains in model 1 (gas mass $M_g = 10 \, M_\oplus$). The grains larger than 100 μm are in the inner part of the gas disk. Their lifetime is order of 1000 times the orbital period $P_{\rm out}$ at $r_{\rm out}(= 100$ AU) and decreases with the size because larger grains inhabit inner part of the disk where the density of colliding grains is higher (eq. [48]). The grains less than 100 μm are in

the edge of the gas disk. At the edge of the disk, the collisional velocity of grains becomes large because the gas density is not high enough for the gas drag force to hold the grains in the same velocity. Thus, the lifetime of these small grains is much shorter than that of larger grains ($s \gtrsim 100$ μm) in the gas disk. In model 1, the lifetime of grains is much larger than the migration time to the steady orbits (the dashed line in Fig. 8a). Thus, the grains spend most of their time in their steady orbits and the dust disk is mainly composed of the grains in the steady orbits. The contribution of grains flowing toward steady orbits to the density of the dust disk or the optical depth can be neglected.

The solid line in Figure 9a shows the optical depth of the dust disk in model 1. The dominant profile of the optical depth is the peak at the edge of the gas disk (~ 90 AU). This peak is made of the grains of $10 \lesssim s_s \lesssim 100$ μm. Because these grains gather in the edge of the gas disk (see Fig. 4), the density of grains becomes high and a dust ring forms there. The lifetime of grains outside the gas disk ($r \gtrsim 100$ AU and $s \lesssim 10$ μm) is much shorter than that of grains in the gas disk. Thus, the optical depth declines steeply outside the gas disk. The large grains ($s_s \lesssim 300$ μm) condense at the innermost part of the gas disk. The density of gas is high at the inner part of the disk, and strong gas drag force suppresses the collisional disruption of grains. Thus, the optical depth at small radius becomes large and an inner dust disk forms at $r \lesssim 40$ AU.

6.5. *Models of Dust Distribution*

The structure of dust disks strongly depends on the properties of gas disks. In this subsection, we show how the structure of the dust disk varies with the variation of the gas disk.

6.5.1. *Small Gas Mass*

The solid line in Figure 8b shows the lifetime of grains in the gas disk with smaller mass (model 2; $M_g = 1 \, M_\oplus$). The lifetime of grains is much shorter than in model 1, because the weaker gas drag force results in high collisional velocity of grains. In model 2 the lifetime is comparable or smaller than the time for the grains to migrate to their steady orbits (the dashed line in Fig. 8b). This means that the dust disk is composed of both the grains in the steady orbits and the grains flowing outward to the steady orbits. Some grains flowing outward are destroyed before arriving at the steady orbits. In this case, the calculation of the density of grains described in § 6.3 is not appropriate. The ring structure at the edge of the gas disk would be less prominent, because some of grains making the ring would be destroyed before arriving at their steady orbits. To obtain the structure of the dust disk, the calculation taking into account the destruction of grains on the way to the steady orbits must be needed. If production rate of grains is 10 times smaller and $\dot{M}_{\rm pro} = 10^{-7} \, M_\oplus \, {\rm yr}^{-1}$, the lifetime of grains is 10 times longer, and our calculation of density would be appropriate. The optical depth in the model of $M_g = 1 \, M_\oplus$ is shown as the dashed line in Figure 9a, assuming that the lifetime of grains are much larger than the migration time. The profile of the optical depth is similar to that in the model of $M_g = 10 \, M_\oplus$, while its magnitude is about 10 times smaller. At the peak of the optical depth in the dust ring ($r \approx 90$ AU), $\tau = 1.1 \times 10^{-1}$ for $M_g = 10 \, M_\oplus$ and $\tau = 1.2 \times 10^{-2}$ for $M_g = 1 \, M_\oplus$.

---

[4] Note that the unit of n_s is cm^{-3}, while that of n' is cm^{-4}.
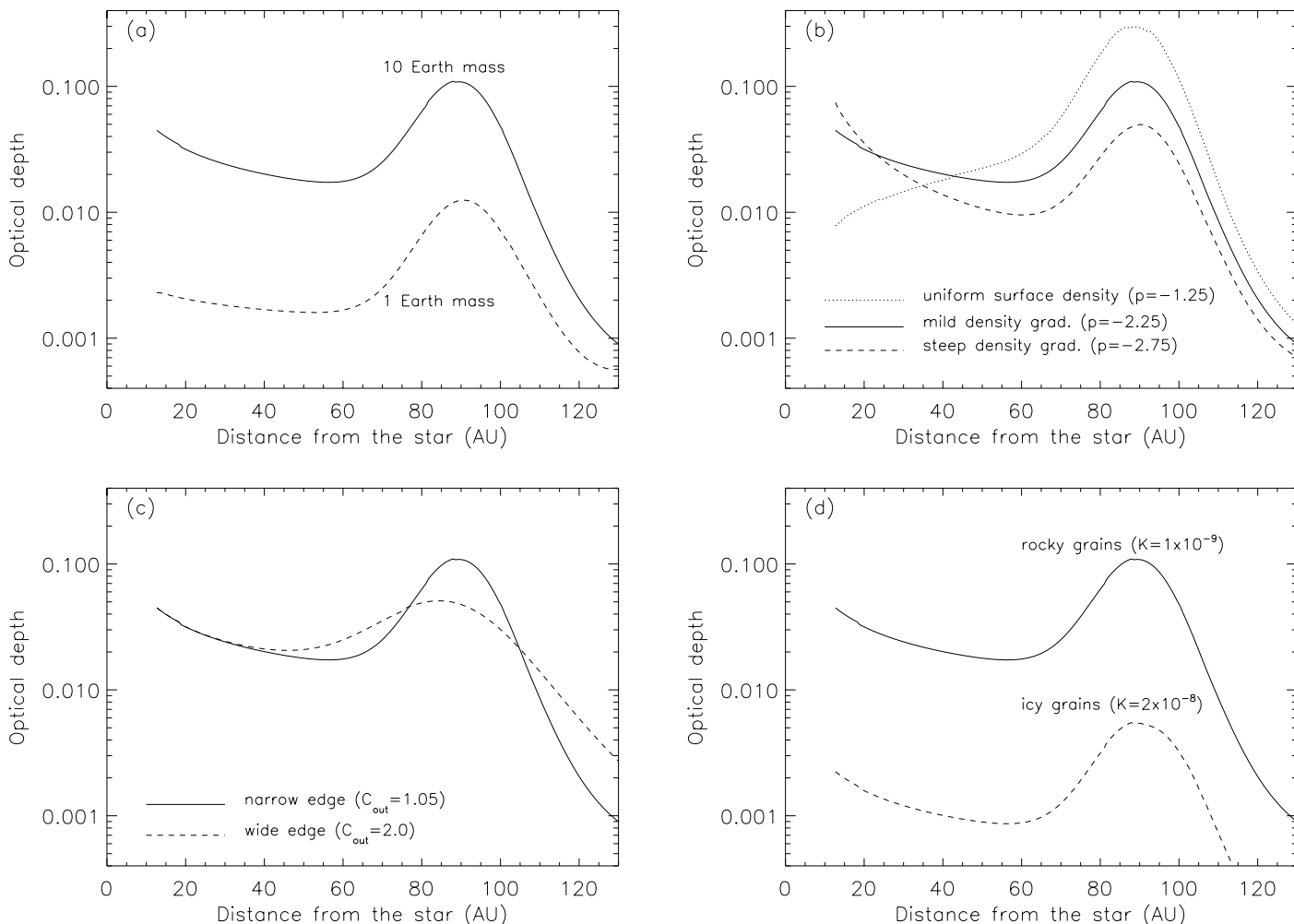
FIG. 9.—The vertical optical thickness (optical depth) of dust disks, calculated using the geometrical cross sections of grains. (a) For various disk masses, M_g. The solid and dashed lines show the optical depth of the dust in the gas disk of 10 $M_\oplus$ (model 1) and 1 $M_\oplus$ (model 2), respectively. (b) For various profiles of gas density, p, where $\rho_g \propto r^p$. The dotted, solid, and dashed lines correspond to $p = -1.25$ (uniform surface gas density; model 4), $p = -2.25$ (model 1) and $p = -2.75$ (model 3), respectively. (c) For various width of the edge of gas disks. The solid and dashed lines correspond to the narrow edge ($C_{out} = 1.05$; model 1) and the wide edge ($C_{out} = 2.0$; model 5), respectively. (d) For various strength of dust grains. The solid and dashed lines correspond to the rocky grains ($K = 1 \times 10^{-9}$; model 1) and the icy grains ($K = 2 \times 10^{-8}$; model 6), respectively.

6.5.2. Different Gas Profiles

In Figure 9b, we show the optical depth of the dust disks for various density gradients of gas disks. The dashed line shows the disk with steeper density gradient (the power-law index of the gas density $p = -2.75$ corresponding to that of the surface density $p_s = -1.5$; model 3). The mass of the gas disk is the same as in model 1 ($M_g = 10 M_\oplus$). Because of the steeper density gradient, the gas density in the inner part of the disk is higher than that in model 1, while the gas density at the edge of the disk is lower. The lower gas density at the edge of the disk causes the shorter lifetime of grains and the smaller optical depth of the dust ring. The grains in the inner part of the disk are strongly held by dense gas. The collisional velocity of these grains are small and collisional destruction of grains is not effective. The grains in the inner part of the disk survive longer than the grains in model 1, and the optical depth increases with decreasing radius r. The inner optically thick disk may obscure the star from the outer part of the disk. In this case, the grains in the outer part of the disk do not experience the radiation pressure force and do not have steady orbits, so that the dust ring would disappear.

The dotted line in Figure 9b shows the disk with constant surface density ($p = -1.25$ and $p_s = 0$; model 4). The gas density in the inner part of the disk is much lower than that in the model 1, while the gas density at the edge of the disk is higher. The optical depth of the dust ring is larger than in the model 1 because of the higher gas density at the edge of the disk. In the gas disk with the constant surface density, even the grains in the innermost part of the disk are not strongly held by gas and are destroyed in short time by collisions with high velocity. The number density of these grains is not as large as that in model 1 or 3. The inner disk is optically thin. In model 4, because the optical depth decreases with decreasing radius r, the inner disk does not obscure the star.

In the previous models, we assumed that the gas disks have sharp outer edges (marginally Rayleigh-stable at the edge where $C_{out} = 1.05$). The sharpness of the edge is not easily observable. Recent images of the dust disk of GG Tau do show a very sharp edge ($\Delta r_{out}/r_{out} \sim 0.04$; Guilloteau, Dutrey, & Simon 1999). However, the edge of gas disk may be much smoother. The optical thickness of the dust disk in the gas disk with a smooth edge ($C_{out} = 2.0$; model 5) is

shown in Figure 9c. The concentration of grains at the disk edge is moderate, and the ring feature is weak.

6.5.3. *Grains of Smaller Collisional Strength*

The efficiency factor of collisional destruction, K, is uncertain (see eq. [43]). If the grains are stronger (weaker), their lifetime is longer (shorter) and their density is higher (lower). As an example, we show in Figure 9d the optical depth of the dust disk with $K = 2 \times 10^{-8}$, which is 20 times larger than K in model 1 and corresponds to the efficiency of collisional destruction of icy grains (model 6). The life-time of the grains is about 20 times shorter than that in model 1, and the optical depth is also 20 times smaller. Icy grains are destroyed more easily than rocky grains and are blown away by the radiation pressure more quickly. There-fore, dust disks are mainly composed of rocky grains with little icy mantle. This is consistent with the properties of the grains derived through the spectral fitting of thermal emis-sion from the HR 4796A dust ring by Augereau et al. (1999b).

7. MORPHOLOGY OF THE RINGED SYSTEMS

We consider first the global quantities (mass and luminosity) of the dust, as well as gas, in the models, and compare them with some observed quantities. Next, we discuss the morphology of the model disks in the thermal and scattered light images.

7.1. *Mass and Luminosity of Model Dust Rings*

The mass of a dust disk M_d is given by

$$M_d = \frac{8}{3} \pi^2 \rho_d \int_{r_{\rm in}}^{r_{\rm out}} r h_d s_s^3 n_s \, dr \; . \tag{55}$$

We set $r_{\rm in} = 50$ AU and $r_{\rm out} = 150$ AU to calculate the mass of the ring part of the disk. The mass of the dust ring in model 1 (gas mass $M_g = 10 \, M_\oplus$) is $9.0 \times 10^{-1} \, M_\oplus$ and the dust mass in model 2 ($M_g = 1 \, M_\oplus$) is $1.0 \times 10^{-1} \, M_\oplus$. The gas to dust ratio is about 10. Thus, the gas-dust coupling affects the motion of gas only slightly, at best. (If dust grains settle down in the mid-plane of the disk, the dust density may exceed the gas density. Even in this case, the dust grains do not affect the gas motion strongly, because of the corotation of gas and dust in steady orbits.)

The above estimate of the mass assumes that the dust ring is composed of grains smaller than $s \sim 200 \, \mu$m. Augereau et al. (1999b) suggested the presence of meter-sized bodies based on the spectral energy distribution of the HR 4796A dust disk. The gas drag and radiation pressure force have little effect on such large bodies, so unlike for the dust component, the distribution of these bodies is not strongly tied to the distribution of gas. The presence of large meteorites and planetesimals (which do not fall under the category of dust) necessarily increases the total mass of the disk of solid matter above our estimate of the dust disk mass. Additional calculations are needed to model the long-term evolution of the large bodies in disks.

The total luminosity of thermal emission and scattered light from the dust ring is

$$L_d = \frac{\pi}{2} L \int_{r_{\rm in}}^{r_{\rm out}} \frac{s_s^2 h_d n_s}{r} \, dr = \frac{1}{2} L \int_{r_{\rm in}}^{r_{\rm out}} \frac{\tau}{r} \, dr \; . \tag{56}$$

The above equation assumes the extinction cross section to be geometrical. The luminosity of the dust ring in model 1 is $1.7 \times 10^{-2} L$ and that in model 2 is $2.0 \times 10^{-3} L$.

The shape of dust rings depends on the sharpness of the edge of gas disks (Fig. 9c). If the edge is more gradual, the ring is wider and its peak density is lower. However, the mass and luminosity of the ring do not strongly depend on the sharpness of the disk edge. In model 5, where the width of the edge is about 2 times wider than that in model 1, the mass and luminosity of the ring are $M_d = 7.2 \times 10^{-1} \, M_\oplus$ and $L_d = 1.4 \times 10^{-2} L$, respectively, which are only about 20% smaller than those in model 1.

We can compare the above numbers with the masses of gas and dust in transitional disks. The HR 4796A dust ring has been observed by thermal emission (Koerner et al. 1998; Jayawardhana et al. 1988; Telesco et al. 2000) and by scat-tered light (Schneider et al. 1999). The emission from the dust ring has a peak around 70 AU (Schneider et al. 1999; Telesco et al. 2000). The luminosities of thermal emission and scattered light are $L_{\rm th} \simeq 5 \times 10^{-3} L$ (Jura 1991) and $L_{\rm sc} \simeq 2 \times 10^{-3} L$ (Schneider et al. 1999), respectively. The total luminosity of the ring is $L_d \simeq 7 \times 10^{-3} L$. A similar dust distribution with a peak at 72 AU and luminosity $L_d \simeq 8 \times 10^{-3} L$ is found in our model 7, where the gas disk has a smooth outer edge at 80 AU and mass $M_g = 4 \, M_\oplus$. The gas mass in model 7, $M_g = 4 \, M_\oplus$, is consistent with the observational upper limit $M_g < 7 \, M_\oplus$ (Zuckerman et al. 1995; Greaves, Mannings, & Holland 2000).

The luminosities of the thermal emission and scattered light of HD 141569A are $L_{\rm th} \simeq 8 \times 10^{-3} L$ (Sylvester et al. 1996) and $L_{\rm sc} \simeq (2–4) \times 10^{-3} L$ (Augereau et al. 1999a; Weinberger et al. 1999), respectively. The total luminosity of the dust is $L_d \simeq 1 \times 10^{-2} L$. The model which reproduces the dust ring with a peak density at 325 AU and luminosity $L_d \simeq 1 \times 10^{-2} L$ has the gas disk with an edge at 370 AU and mass $M_g = 50 \, M_\oplus$ (model 8). The inferred gas mass is consistent with the mass $M_g \simeq 20–460 \, M_\oplus$ derived by the observation (Zuckerman et al. 1995).

Although the gas masses derived by our models are con-sistent with the observations, we must note that any exact match could be accidental. Our models have large uncer-tainties. In particular, the efficiency of the collisional destruction K has an order of magnitude of uncertainty (eq. [43]). If K of the actual grains were larger/smaller than the value we adopted ($K = 1.0 \times 10^{-9}$), then the grains would be more/less easily destroyed and the mass and luminosity of dust in a given gas disk would be lower/higher.

7.2. *Model Images of Scattered and Thermal Radiation*

In Figure 10 we present the theoretical image of model 4 (constant gas surface density), inclined to the line of sight by $60°$ from pole-on, in the near-IR scattered light (gray-scale brightness map at 1.1 μm wavelength) and the mid-IR thermal radiation (overplotted contours of the 18.2 μm flux). Our modeling is somewhat simplistic, in that the scat-tering function is assumed to be isotropic (which does not alter the general morphology, just removes any up-down asymmetry of the theoretical image). However, the tem-perature profile as a function of radius needs to be com-puted as accurately as possible for a reliable prediction of thermal IR flux distribution, so we compute it within Mie theory, from the assumed properties of grains (specified earlier in § 2).

The dust morphology in the model is qualitatively similar to those inferred from observations of the transitional system HD 141569A. The 18.2 μm flux is centrally concen-trated (like that imaged by Fisher et al. 2000), while the
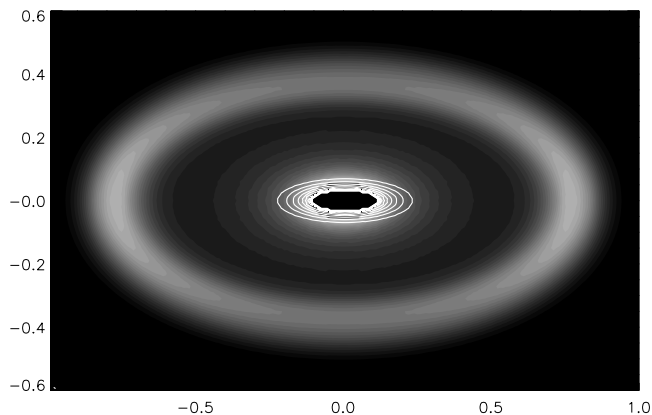
FIG. 10.—Simulated image of model 4 disk in the scattered light and thermal emission. The gray scale shows the scattered light flux at 1.1 μm with linear spacing. The contours show thermal flux at 18.2 μm and are spaced linearly. Units of flux are arbitrary. The disk has a constant surface density of gas with an edge at 100 AU, viewed 60° from pole-on. The flux is calculated for $r \geq 13$ AU (outside the artificial hole at the center).

scattered light shows two separate components: the inner disk and the outer ring, with the brightest parts being the two projection-enhanced ansae. If these two components are largely overlapping, they may create the impression of a shallow gap, resembling qualitatively the image at $\lambda \approx 1.1$ μm by Weinberger et al. (1999). (However, see Augereau et al. 1999a for the dust distribution from their observations at $\lambda \approx 1.6$ μm.) The model disk in Figure 10 has a constant gas surface density with a downturn beyond 100 AU. Model disks with surface density increasing with decreasing radius (model 1, etc.) show much more prominent inner disks both in scattered light and in thermal emission. Comparison with the observations suggests that gas is not concentrated in the inner part of the disk. The flat profile of gas surface density might arise after the viscous evolution.

In order to achieve a quantitative agreement of our models with the observations of HD 141569A, we would need to (1) consider nonisotropic scattering function, (2) allow for a more gradual outer gas truncation, and (3) convolve the theoretical images with the appropriate point-spread functions. As already mentioned, we defer the comprehensive modeling of individual objects to a subsequent paper.

Another system that might be qualitatively described by our dust migration models, HR 4796A, show a enhanced-brightness ansae of the dust ring in scattered light (Schneider et al. 1999), similar to our model in Figure 10. The 18.2 μm images also indicate a ringlike morphology (Koerner et al. 1998; Jayawardhana et al. 1998; Telesco et al. 2000). In other words, the dust ring with characteristic radius of 70 AU, producing the scattered light, also produces most of the 18.2 μm thermal radiation. Our thermal mid-IR map shows a more centrally concentrated morphology, therefore our modeling procedure needs to be argued in order to fit the observations. Two possibilities exist. First, our model image represents the emission from dust in steady circular orbits and omits the possible contribution by other particles, those flowing out on spiral orbits due to $\beta > 1$, and the ones pumped up to high eccentricity at the edge of the disk (see § 5.2). The combined area of such dust grains is small, but they could in principle be seen because of the small physical sizes and the associated higher temperatures (see Fig. 4 in Augereau et al.

1999b and Fig. 5 in Wyatt et al. 1999). We note that the thermal emission in mid-IR (the Planck function in Wien regime) and thus the visibility of grains in the outer ring is often very sensitive to the dust grain temperature; it is not uncommon to find that the predicted 18.2 μm flux from the ring becomes 6 times under just ~20% increase in dust temperature (from 70 to 84 K), which could make the model ring visible. Another way to assure a quantitative fit to HR 4796A data is a modification of the modeled gas profile, which depletes the gas inside the ring radius. Our model would then produce a more sharply defined ring and less dust inside the ring, because, at the region where gas is depleted, collisional disruption of dust grains is violent. This depletion of gas (and dust) might in this case be due to one or more planets or a low-mass companion inside about a half of the ring radius (~40 AU).

8. DISCUSSION AND SUMMARY

8.1. *Dust Morphologies and Their Observability: Implications for Gas*

As shown in § 6.5, a variety of dust morphologies can be obtained in our models with deliberately smooth (monotonic) gas distributions, depending on how wide and dense the outer ring is relative to the inner disk. For instance, there might exist systems with ring morphology, ring plus inner disk morphology (possibly giving impression of disks with gaps), and disks with weak/unobservable rings. Our models can predict IR (scattered and thermal) images and spectral energy distributions, as an example of IR images is shown in § 7.2. We can deduce the properties of gas disks by comparing these model images with the dust observations. In this subsection, we discuss the implications for observations of dust and gas disks.

When the model of the gas disk and dust properties (the radiation pressure strength β vs. size s) are given, the density and size distributions of dust are predicted by our model. The predicted distributions depend strongly on the density profile of the gas disk, as shown in § 6.5.2, while the dependence on the temperature profile is not strong and the chemical properties of the gas (e.g., abundance of heavy elements) affect little of the predicted dust density. Hence, the deduced density profiles of gas disks through the comparison with the dust observations provide complementary information to the direct observations of gas, such as ^{12}CO molecular lines (which depend on the abundance ratio of CO to H_2) and H_2 molecular lines (which depend strongly on the temperature of the gas).

It is straightforward to obtain IR images of the model disks, because the size distribution and temperature profile of dust can be calculated by our models. The near-IR (scattered) light traces the density distribution of dust. The ring structure would be prominent in near-IR and indicates the radius of the gas disk and width of the disk edge. On the other hand, the mid- to far-IR (thermal) emission traces temperature structure. For example, the mid-IR emission is sensitive to the hot dust near the star, as shown in Figure 10. By taking images of dust disk from near- to far-IR, we can deduce both the density and temperature profiles of dust. Comparing dust density profile with our models provides the inferred gas density profile. Then, from the dust temperature profile, we can find the size distribution of dust as a function of the distance from the star, because the dust temperature depends on the grain size. Comparison of grain

size distributions inferred by the observations with those predicted by our models gives us information of dust properties, such as composition, porosity, state (amorphous or crystalline) etc. From the information of dust grains, we can explore the stage of dust evolution and planetary formation. This procedure can be applied to transitional disks on the way of gas dissipation, which are optically thin and with moderate gas mass (1–100 $M_\oplus$). Therefore, by taking IR images of dust disks around stars with various ages, we can investigate the evolution of gas disks, especially the dissipation of gas, which limits the timescale of formation of gas giant planets, as well as the evolution of dust grains.

The observations of H_2 molecule lines in mid-IR provide direct and independent information of gas density and temperature profiles (Thi et al. 2001). Although observations of gas are more difficult than those of dust, future space missions such as SIRTF will reveal the properties of gas disks. When we obtain the density and temperature profiles of both the gas and dust disks by the direct observations, our model will be tested by these observations. If the dust migration cannot explain the observations, the other mechanisms of forming structure of dust disks, such as sculpting planets, will have a strong support.

8.2. Origin of Structure in Disks: Dust Migration vs. Extrasolar Planets

Our results also bear on the timely issue of planet detection in extrasolar systems. Radial and azimuthal structure can be induced in circumstellar disks by the gravitational perturbation due to planets or other substellar companions in or in the vicinity of disks (see Dermott et al. 1994, Liou & Zook 1999, Wyatt et al. 1999, and Ozernoy et al. 2000 for gas-free disks, and, e.g., Lubow et al. 1999 for gas disks). Detection of such structure is one of the main diagnostic tools in many of the future imaging projects at various wavelengths. However, caution should be exercised while interpreting disk morphology. There are many possible reasons unrelated to dynamical perturbations that could, in principle, masquerade as planets (Artymowicz 2000).

First, optically thick disks with radius-dependent thickness might cast shadows on parts of themselves. Next example would be a recent collision of planetesimals in disk. Though the cloud of dust released in such a collision would not be observable, it might become observable if exponentially amplified in the so-called dust avalanche (Artymowicz 1997, 2000). This requires the optical thickness in the disk mid-plane larger than that in the β Pic disk (transitional disks satisfy this requirement, as a rule). While admittedly rare and improbable, such a collision might produce dense patches or sectors in a disk, which are nonaxisymmetric and time-dependent on orbital timescale, features similar to those offered by dynamical sculpting. Another example is the dust migration, potentially much more common, but fortunately easier to distinguish from planetary influences.

Dust migration is capable of sculpting the disks, with an important difference from dynamical sculpting that it cannot itself produce nonaxisymmetry. It can, however, provide an alternative explanation of some observed features, especially the radially structured dust disks, rings, and apparent gaps in disks. By carefully analyzing the axisymmetry (or lack thereof) of the underlying dust distribution, taking properly into account the asymmetry of the image due to the nonisotropic scattering function of a collection of dust grains, the observers will be able to decide whether or

not our intrinsically axisymmetric models apply to any observed system. If axisymmetric model reproduce the observations and the inferred gas amount does not clash with any observational constraints, then the dust migration hypothesis is preferred over the planetary hypothesis by the virtue of being more natural (conservative). This is especially true in systems where gas has been independently detected.

It appears that a convincing planet detection by way of dust imaging should include not just a nonaxisymmetric (and time-dependent) structure in the disk, but a very specific one, closely following the predictions of numerical simulations of either gas-free or gas-rich disks.

8.3. Summary

We have studied in the present paper the combined action of gas drag and radiation pressure on dust grains in optically thin circumstellar gas disks. Our results on the migration and structure formation of dust are as follows.

1. Grains can migrate inward or outward, depending on whether their azimuthal motion is faster or slower than the rotation velocity of gas. Even the grains smaller than the blow-out radius (with $\beta > 1$) will typically have spiral trajectories in gas disks.

2. We have provided analytical formulae for the radial migration speed, which agree with the detailed numerical integrations. For grain sizes $0.1 \lesssim s \lesssim 10$ μm in disks around A-type stars of radius comparable with 100 AU and masses of order 1–10 Earth masses, the radial migration speed is comparable with the gas sound speed.

3. A particle may reach a stable equilibrium orbit, where it corotates with the gas. The equilibrium orbital radius depends on the grain size. That dependence is determined by the rotation curve of the gas disk, depending on the radial gas distribution. Smaller grains normally find a steady orbit farther from the central star. This results in the fractionation of grains according to their sizes.

4. The eccentricity of a grain is strongly damped throughout most of the disk but is excited at the edge of the gas disk, where the gas density falls rapidly. Rule number 3 above applies then, not to the whole orbit, but to the vicinity of the pericenter of the orbit.

5. We have studied gas disk models with density varying as a power law, truncated within a scale length comparable with the disk scale height, and a total mass from a fraction to dozens of Earth masses. The outcome of grain migration depends on the radiation pressure coefficient β and the grain size.[5] The fine dust fraction ($\beta \gtrsim 0.5$; $s \lesssim 5$ μm) is removed by strong radiation pressure. Dust grains with $0.1 \lesssim \beta \lesssim 0.5$, or alternatively $5 \lesssim s \lesssim 20$ μm, form an extended, outer dust disk component, residing most of the time beyond the bulk of the gas disk on eccentric orbits. Grains of intermediate size ($0.01 \lesssim \beta \lesssim 0.1$ or 20μm $\lesssim s \lesssim 200$ μm) concentrate near the outer edge of the gas disk, forming a prominent dust ring of width similar to the scale length of gas density cutoff. Sand grains ($\beta \lesssim 0.01$, $s \gtrsim 200$ μm) gather in the inner part of the gas disk.

6. The density profiles of dust disks are calculated by considering the balance between the supply and removal of

---

[5] The primary dependence is on β. The approximate ranges of grain radii are cited below for $\beta(s)$ based on our physical model of grains and for the luminosity to mass ratio of the star equal 8.4 times the solar value, as appropriate for HR 4796A and approximately also for HD 141569A.

grains through collisional destructions. The dust density has a different profile from that of gas and has a peak at the edge of the gas disk. This density enhancement is observed as a ring in the near-IR scattered light. The width and the contrast of the ring relative to the inner part of the disk depend on the properties of gas disk. Therefore, we can derive the properties of gas disks, e.g., mass and density profiles, from the observations of dust disks.

7. We have compared our models with two observed transitional disks around HR 4796A and HD 141569A. The model images of scattered (near-IR) and thermal (mid-IR) radiation qualitatively agree with most of the observed characteristics of these disks, especially around HD 141569A.

REFERENCES

Adachi, I., Hayashi, C., & Nakazawa, K. 1976, Prog. Theor. Phys. 56, 1756
Arakawa, M. 1999, Icarus, 142, 34
Artymowicz, P. 1988, ApJ, 335, L79
———. 1997, Annu. Rev. Earth Planet. Sci., 25, 175
———. 2000, Space Sci. Rev., 92, 69
Artymowicz, P., & Clampin, M. 1997, ApJ, 490, 863
Augereau, J. C., Lagrange, A. M., Mouillet, D., & Ménard, F. 1999a, A&A, 350, L51
Augereau, J. C., Lagrange, A. M., Mouillet, D., Papaloizou, J. C. B., & Grorod, P. A. 1999b, A&A, 348, 557
Boss, A. P. 2000, ApJ, 536, L101
Brouwer, D., & Clemence, G. M. 1961, Methods of Celestial Mechanics (New York: Academic)
Burns, J. A., Lamy, P. L. & Soter, S. 1979, Icarus, 40, 1
Dermott S. F., Jayaraman, S., Xu, Y. L., Gustafson, B. A. S., & Liou, J. C. 1994, Nature, 369, 719
Dorschner, J., Begemann, B., Henning, Th., Jäger, C., & Mutschke, H. 1995, A&A, 300, 503
Dunkin, S. K., Barlow, M. J., & Ryan, S. G. 1997, MNRAS, 290, 165
Fisher, R. S., Telesco, C. M., Piña, R. K., Knacke, R. F., & Wyatt, M. C. 2000, ApJ, 532, L141
Grady, C. A., et al. 2000a, ApJ, 544, 895
Grady, C. A., Sitko, M. L., Russell, R. W., Lynch, D. K., Hanner, M. S., Pérez, M. R., Bjorkman, K. S., & de Winter, D. 2000b, in Protostars and Planets IV, ed. V. Mannings, A. P. Boss, & S. S. Russell (Tucson: Univ. Arizona Press), 613
Greaves, J. S., et al. 1998, ApJ, 506, L133
Greaves, J. S., Mannings, V., & Holland, W. S. 2000, Icarus, 143, 155
Guilloteau, S., Dutrey A., & Simon, M. 1999, A&A, 348, 570
Hayashi, C. 1981, Prog. Theor. Phys. Suppl., 70, 35
Hayashi, C., Nakazawa, K., & Nakagawa, Y. 1985, in Protostars and Planets II, ed. D. C. Black & M. S. Matthews (Tucson: Univ. Arizona Press), 1100
Hillenbrand L. A., & Meyer, M. 1999, BAAS, 195, 02.09
Holland, W. S., et al. 1998, Nature, 392, 788
Hollenbach, D. J., Yorke, H. W., & Johnstone, D. 2000, in Protostars and Planets IV, ed. V. Mannings, A. P. Boss, & S. S. Russell (Tucson: Univ. Arizona Press), 401
Holsapple, K. A. 1993, Annu. Rev. Earth Planet. Sci. 21, 333
Housen, K. R., & Holsapple, K. A. 1990, Icarus, 84, 226
———. 1999, Icarus, 142, 21
Jayawardhana, R., Fisher, S., Hartmann, L., Telesco, C., Piña, R., & Fazio, G. 1998, ApJ, 503, L79
Jura, M. 1991, ApJ, 383, L79
Jura, M., Malkan, M., White, R., Telesco, C., Pina, R, & Fisher, R. S. 1998, ApJ, 505, 897
Jura, M., Zuckerman, B., Becklin, E. E., & Smith, R. C. 1993, ApJ, 418, L37

Kenyon, S. J., Wood, K., Whitney, B. A., & Wolff, M. J. 1999, ApJ, 524, L119
Klahr, H. H., & Lin, D. N. C. 2001, ApJ, 554, 1095
Koerner, D. W., Ressler, M. E., Werner, M. W., & Backman, D. E. 1998, ApJ, 503, L83
Kwok, S. 1975, ApJ, 198, 583
Lagage, P. O., & Pantin, E. 1994, Nature, 369, 628
Lagrange, A. M., Backman, D. E., & Artymowicz, P. 2000, in Protostars and Planets IV, ed. V. Mannings, A. P. Boss, & S. S. Russell (Tucson: Univ. Arizona Press), 639
Laughlin, G., & Bodenheimer, P. 1994, ApJ, 436, 335
Lecavelier des Etangs, A., Vidal-Madjar, A., & Ferlet, R. 1998, A&A, 339, 477
Liou, J.-C., & Zook, H. A. 1999, AJ, 118, 580
Liseau, R., & Artymowicz, P. 1998, A&A, 334, 935
Lissauer, J. J. 1993, ARA&A, 31, 129
Lubow, S. H., Seibert, M., & Artymowicz, P. 1999, ApJ, 526, 1001
Meyer M. R., & Beckwith, S.V.W. 2000, in ISO Surveys of a Dusty Universe, ed. D. Lemke, M. Stickel, & K. Wilke (Heidelberg: Springer),
Natta, A., Grinin, V. P., & Mannings, V. 2000, in Protostars and Planets IV, ed. V. Mannings, A. P. Boss, & S. S. Russell (Tucson: Univ. Arizona Press), 559
Osterloh, M., & Beckwith, S. V. W. 1995, ApJ, 439, 288
Ozernoy, L. M., Gorkavyi, N. N., Mather, J. C., & Taidakova, T. A. 2000, ApJ, 537, L147
Pantin, E., Lagage, P. O., & Artymowicz, P. 1997, A&A, 327, 1123
Roques, F., Scholl, H., Sicardy, B., & Smith, B. A. 1994, Icarus, 108, 37
Schneider, G., et al. 1999, ApJ, 513, L127
Stauffer, J. R., Hartmann, L. W., & Barrado y Navascues, D. 1995, ApJ, 454, 910
Sylvester, R. J., Skinner, C. J., Barlow, M. J., & Mannings, V. 1996, MNRAS, 279, 915
Telesco, C. M., et al. 2000, ApJ, 530, 329
Thi, W. F., et al. 2001, Nature, 409, 60
van den Ancker, M. E., de Winter, D., & Tjin A Djie, H. R. E. 1998, A&A, 330, 145
Weidenschilling, S. J. 1977, MNRAS, 180, 57
Weinberger, A. J., Becklin, E. E., Schneider, G., Smith, B. A., Lowrance, P. J., Silverstone, M. D., Zuckerman, B., & Terrile, R. J. 1999, ApJ, 525, L53
Weinberger, A. J., Rich, R. M., Becklin, E. E., Zuckerman, B., & Matthews, K. 2000, ApJ, 544, 937
Wyatt, M. C., Dermott, S. F., Telesco, C. M., Fisher, R. S., Grogan, K., Holmes, E. K., & Piña, R. K. 1999, ApJ, 527, 918
Zuckerman, B., & Becklin, E. E. 1993, ApJ, 414, 793
Zuckerman, B., Forveille, T., & Kastner, J. H. 1995, Nature, 373, 494